UNIVERSIDADE D COIMBRA
FACULDADE DE CIÊNCIAS E TECNOLOGIA

João Bernardes Guerreiro

Beryllium oxide for semiconductor technology

Thesis submitted to the
University of Coimbra for the degree of
Master in Engineering Physics

Supervisor:
Prof. Dr. Rui Vilão

Coimbra, 2018

Aos meus pais

Acknowledgments

Em primeiro lugar queria agradecer ao meu orientador, o Professor Dr. Rui Vilão, por tudo que me ensinou durante este projeto, pela entrega e disponibilidade total que demonstrou ao longo deste ano e por me ter dado a oportunidade de integrar um grupo de investigação científica. Queria também extender este agradecimento a todo o grupo de investigação de muões em Coimbra e ao departamento de física por me terem proporiconado a oportuindade de participar na atividade experimental no Reino Unido, que foi uma experiência incomparável.

Queria agradecer a toda a minha família pelas oportunidades que me proporcionaram e pelo apoio incondicional que sempre me deram durante todas as minhas etapas de vida. Sem eles nada disto era possível.

Queria ainda agradecer aos meus amigos por todos os momentos que partilhámos no nosso precurso académico. Sejam eles fáceis como jogar copas no BM ou mais complicados como este mesmo em que estamos todos a terminar o curso. São memórias que sempre me acompanharão.

Resumo

Investigámos o hidrogénio como impureza no óxido de berílio usando a espectroscopia do spin do muão. No primeiro capítulo expomos vários problemas derivados da continua diminuição de escala dos transistores. Como principais causas destes, destacamos efeitos de túnel quântico e defeitos na rede. Estudos comprovam que o BeO é um material promissor no que toca a mitigar estes problemas. O hidrogénio é uma impureza abundante em oxidos e o BeO não é exceção. Isto pode ser prejudicial para a operação de futuras aplicações tais como tecnologia cmos (complimentary metal-oxide-semiconductor). O hidrogénio como impureza no BeO está mal caracterizada e esse passa pelo objetivo principal desta dissertação. De forma a concretizar este objetivo utilizámos a técnica de espetroscopia do muao onde se usa o muão positivo para imitar o comportamento dos protões. A atividade experimental foi levada a cabo no ISIS, Reino Unido. Lá, investigámos a dependência do sinal μSR com a temperatura usando um campo magnético transverso ao spin dos muões. Tirámos também medidas de campo longitudinal numa tentativa de restaurar a polarização inicial dos muões e assim estimar a interação hiperfina. Para além disto usamos uma técnica chamada *quadrupole avoided level-crossing* de forma a caracterizar a posição ocupada pelo muão. Caracterizámos uma configuração dadora e aceitadora do hidrogénio no BeO. Em particular, a configuração dadora é atribuída ao muão positivo numa posição ligante ao oxigénio. A configuração aceitadora é atribuída ao muónio neutro intersticial. Aplicámos ao BeO um modelo emergente para a formação de muónio em óxidos. De acordo com este, o muónio tem de passar por um estado de transição antes de chegar a uma configuração final estável.

Keywords: Hidrogénio, Muónio, espectroscopia do spin do muão, BeO

Abstract

We have investigated the hydrogen impurity in beryllium oxide using muon spin spectroscopy. In the first chapter we lay out several problems that arise from the continuing downscale of transistors. We highlight tunneling and lattice defects as the main causes of this. Studies have shown that BeO is a promising material with respect to solving these issues. Hydrogen is an abundant impurity in oxides and BeO is no exception. This may be detrimental to the operation of future applications such as cmos (complimentary metal-oxide-semiconductor) technology. The hydrogen impurity in BeO is poorly characterized and this is the main objective of this dissertation. To do this we use the muon spin spectroscopy technique in which the positive muon is used to mimic the behavior of the protons. The experimental work took place at ISIS, UK. There we investigated the dependence of the μSR signal with temperature using a transverse magnetic field (to the initial spin polarization). We also took longitudinal field measurements in an attempt at restoring the initial polarization of the muons and thus estimate the hyperfine interaction. Furthermore we made use of a technique called quadrupole avoided level-crossing in order to attempt a characterization of the muon site. We characterized the donor and acceptor configurations of the hydrogen in BeO. In particular the donor configuration is attributed to the positive muon in an oxygen bound position. The acceptor configuration is attributed to interstitial neutral muonium. We apply to BeO an emerging model for muonium formation in oxides, according to which, muonium must go through a transition state before reaching a stable final configuration.

Keywords: Hydrogen, Muonium, Muon spin spectroscopy, BeO

List of Figures

List of Tables

Contents

1

Introduction

1.1 Moore's law and the need of high-κ dielectrics in microelectronics

> "The future of integrated electronics, is the future of electronics itself."
> Gordon Moore, 1965

In 1965, Gordon E. Moore, who at the time was director of the semiconductor division of Fairchild, published a paper that aimed to explain the advantages of integrated electronics as well as predict some of its applications. In this work, he stated that in 1975, 10 years later, there would be approximately 65000 electronic components on a single chip which would translate into a two fold increase every year from 1965 onwards. This exponential growth trend has since become known as Moore's Law[1][Moo65].

This was an extremely bold prediction, at the time, which remained accurate up until recent years (Fig. 1.1). Nowadays computer processing chips can hold up to billions of transistors [Rub16]. In order to do so, these components are constantly decreasing in size. In fact, a limit is being reached where shrinking them further than the nanometer (10^{-9} m) becomes impossible as the atomic scale is being reached. Besides this, the continuous downscale of microelectronics is no longer cost effective and carries lots of unintended side effects like current leakage [Sim16a]. Basically,

[1]This was later revised by Moore himself where he adjusted his component growth to double every two years

Moore's Law is starting to see its days out [Sim16b].

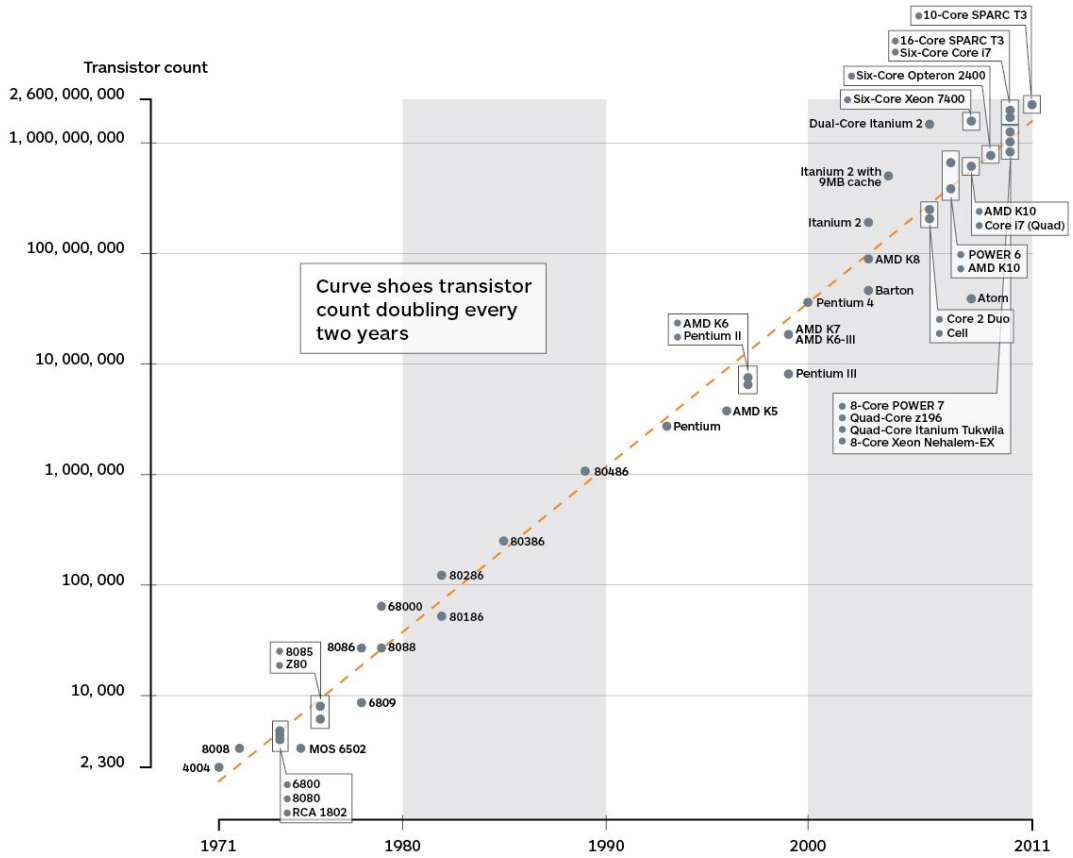

Figure 1.1: Semilogarithmic plot of the transistor count with respect to time, Moore's exponential growth prediction is depicted by the dashed line. Extracted from [Sch15]

The following figure represents the MOSFET (metal-oxide-semiconducting field effect transistor).

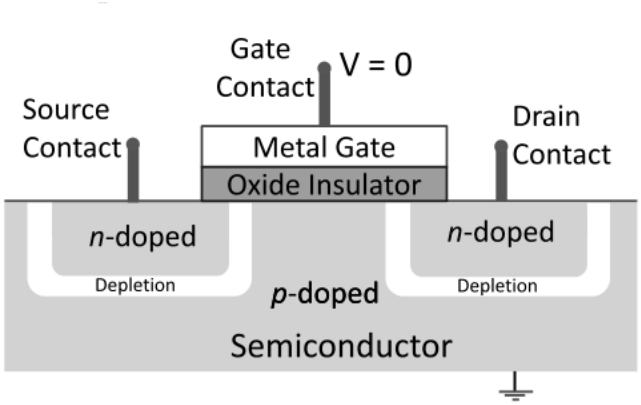

Figure 1.2: A scheme of a MOSFET (n-type) with its layers, extracted from [Sim13].

In MOSFETs like the one presented above, the oxide layer acts as the dielectric material on a parallel plate capacitor whose walls are the gate and the substrate, which is usually composed of doped silicon, germanium or a III-V doped semiconductor.

When scaling down the size of transistors to the nanometer scale (10^{-9} m) quantum mechanics start to come into play. In this realm, particles can step out of their classical boundaries through quantum tunneling which becomes detrimental to the performance of transistors. The tunneling probability between the gate and the substrate increases as thickness is reduced. This implies that scaling down the size of MOSFETs means that a balance must be struck between slimming down the oxide layer whilst preventing current leakage.

The classical gate oxide is SiO_2 which has several favorable properties. It can be thermally grown in silicon which results in a reduced density of intrinsic defects between the SiO_2/Si (oxide/substrate) junction. It also acts as a great insulator with a band gap of $\sim$ 9 eV and is thermally stable. Tunneling, for a SiO_2/Si junction occurs at around 3 nm, depending on the operating power of the circuit [Hou03].

By inspecting equation 1.1 it is evident that by using a high-κ dielectric material one can afford a thicker gate oxide for the same capacitance, thus reducing current leakage.

$$C = \kappa\epsilon_0\frac{A}{d} \tag{1.1}$$

- C is the capacitance
- κ is the dielectric constant
- ϵ_0 is the perimittivity of vacuum (8.85×10^{-12} F m^{-1})
- A is the area of the plate
- d is the thickness of the dielectric

As technology evolved, the classical SiO_2 insulator started being replaced by high-κ metal oxide materials like HfO_2, ZrO_2 and Al_2O_3. However, depositing these

materials on silicon or any III-V substrate will carry lots of unintended defects which can and will create problems regarding current leakage.

In silicon based MOSFETS, HfO_2 has a very high defect density on the junction. Here, the vacancy of oxygen allows the formation of energy levels near the conduction band of Si, enabling carrier diffusion [XRGC05]. In materials like Al_2O_3, $SrTiO_3$, Ta_2O_5, a low-κ interfacial layer (Fig. 1.3) can be formed [WWA01]. This poses a problem because it compromises capacitance and therefore thickness. In fact, as equation 1.2 demonstrates, the total capacitance will correspond, in approximation, to the unintended low-κ capacitance, considering $C_{h\kappa} >> C_{l\kappa}$.

$$\frac{1}{C_{total}} = \frac{1}{C_{h\kappa}} + \frac{1}{C_{l\kappa}} \Leftrightarrow C_{total} = \frac{C_{h\kappa} \times C_{l\kappa}}{C_{h\kappa} + C_{l\kappa}} \sim C_{l\kappa} \tag{1.2}$$

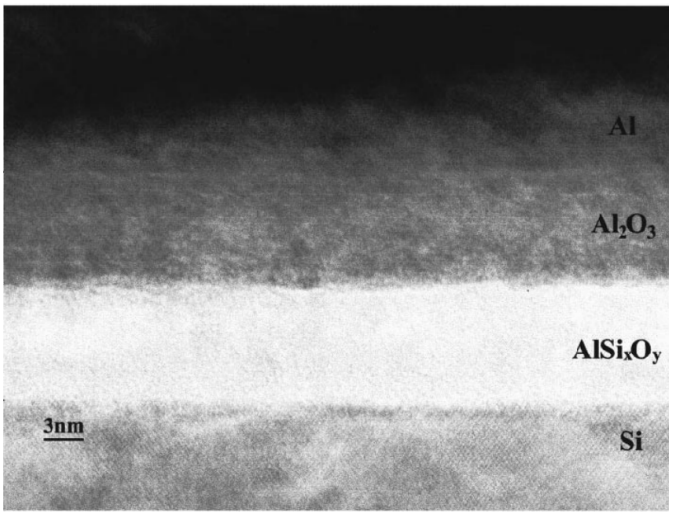

Figure 1.3: The low-κ interfacial layer for a high-κ dielectric, Al_2O_3, from [WWA01].

In III-V substrates defects are also very pronounced. Contrary to silicon, there are no apparent high quality analogue oxides for the gate dielectric role, which means growth techniques like atomic layer deposition have to be implemented leaving room for lots of possible lattice imperfections. The band gap for many different oxides becomes lower on the junction due to these defects, allowing the diffusion of charge carriers to the dielectric [RF06]. The implementation of an interface passivation layer

between the oxide and the substrate is being touted as a solution to the problem presented above [YSH+12].

One of the most promising materials for the passivation layer role is beryllium oxide. This is due to the fact that it has a high dielectric constant (6.8 [YBH+14]), band gap (10.58 eV [MVV+17]) and is thermodynamically stable along with silicon. The Si/BeO junction was proven to reduce leakage currents when compared to HfO_2 and Al_2O_3 [MVV+17]. A thin layer of BeO between Al_2O_3 and silicon may therefore prevent the formation of the thin low-κ $AlSi_xO_y$ interfacial layer. Moreover, BeO is also being studied as a possible substitute for HfO_2 as the gate oxide, in high power applications [JYH+14]. Precautions must be taken when handling this material, especially powder BeO samples due to its toxicity.

1.2 Hydrogen in Oxides

Like all materials, BeO carries impurities and defects that can affect its implementation as a high-κ dielectric.

Out of all impurities it is important to highlight hydrogen. It is extremely common and bound to appear during the growth phase of the material. Hydrogen concentration in thin films of atomic layer deposited BeO was found to be up to 5 % which constitutes an electrically relevant amount [YBH+14].

The ability for hydrogen to easily bond with other atoms allows it to combine with other impurities and create a new defect with its own electric properties: either removing unintended defect levels from the band gap (passivation) or introducing new energy levels altogether (activation). One of the most prominent examples of this is in amorphous silicon. Here, hydrogen passivates the defects and removes parasitic energy levels, widening the band gap and opening the door for applications such as solar cells or thin-film transistors [dWCN03].

Isolated hydrogen can also act as a compensating impurity due to its usual amphoteric nature, acting as a donor on a p type semiconductor or as an acceptor on a

n-type [Vil07]. In some other cases, like in ZnO, hydrogen can even act as the main dopant responsible for n-type conductivity [dWC00].

Hydrogen can then strongly impact the conduction properties of oxides. It is therefore of the uttermost importance to understand precisely how it behaves inside BeO before using it in any electronic application [Alb17] [Vil07]. This is the motivation behind the work presented in this essay.

1.3 Hydrogen in BeO: state of the art

Despite being a rather exotic technique, muon spectroscopy has established itself as the standard procedure to access the behavior of hydrogen in oxides.

These experiments use the muon as an analogue to hydrogen. The muon can capture an electron and form muonium which acts as the hydrogen atom analogue (H). This will be explained with further detail in section 2.1.1.

The accumulated experimental information on hydrogen in BeO is very scarce and limited to muon spin spectroscopy results. S.F.J. Cox et al described the presence of muonium in several high-κ dielectrics, including BeO [CGL$^+$06]. The characterization of muonium state in BeO has been performed at the Paul-Scherrer institute [Vie18] [MVV$^+$17].

The aim of this work was therefore to characterize the behavior of the positively charged H^+ configuration in BeO by using its analogue, the positive muon particle. We have performed μSR experiments at the ISIS facility, UK, in September 2017, which thus constitute the bulk of this thesis. The data here presented will be composed of temperature and magnetic field measurements. All of our results as well as their analysis and ensuing discussion is present in chapter 4.

Ab-initio theoretical calculations

Here, some state of the art theoretical predictions are presented regarding the most thermodynamically stable states for H^+ and H^0 (protium) in BeO, based on *ab-initio* calculations performed by A. Marinopoulos [MVV+17].

BeO crystallizes in a hexagonal wurtzite structure at normal conditions. Hydrogen can find a plethora of different configurations inside a structure like this. In figure 1.4 it is possible to see the crystal structure of the material as well as the most likely stopping sites for hydrogen which were taken as the initial sites for the calculations.

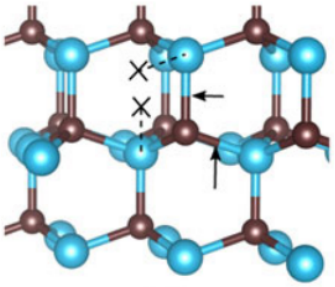

Figure 1.4: The ideal wurtzite structure of the BeO crystal. The blue and black spheres correspond to the Oxygen and Beryllium atoms respectively. The × symbol corresponds to the anti-bonding oxygen (AB−O) sites and the arrows to the bond center (BC) sites. From [MVV+17]

The following configurations correspond to the states occupied by the Hydrogen ion, H^+. The calculated ground state is depicted in Fig. 1.5. In Fig. 1.6 are the higher energy metastable configurations found in the theoretical calculations.

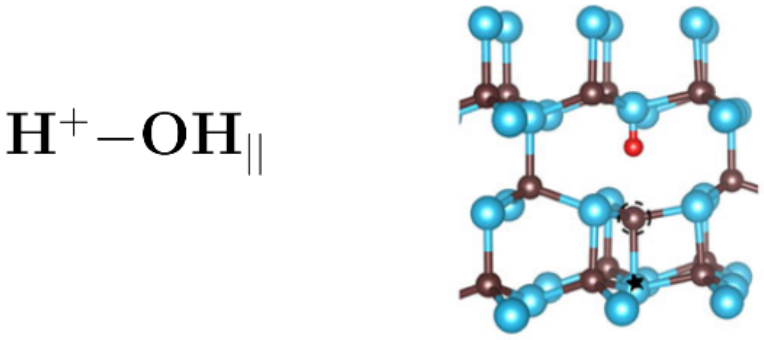

Figure 1.5: Computed ground state configuration for H^+. Note the Hydrogen nucleus is the little red sphere. The dashed circled atom correspond to the lattice atom that was replaced by the impurity and is left unpaired. It will therefore bond with a different atom than the one predicted initially. This atom is indicated by the star. This causes a defect in the lattice. Adapted from [MVV+17]

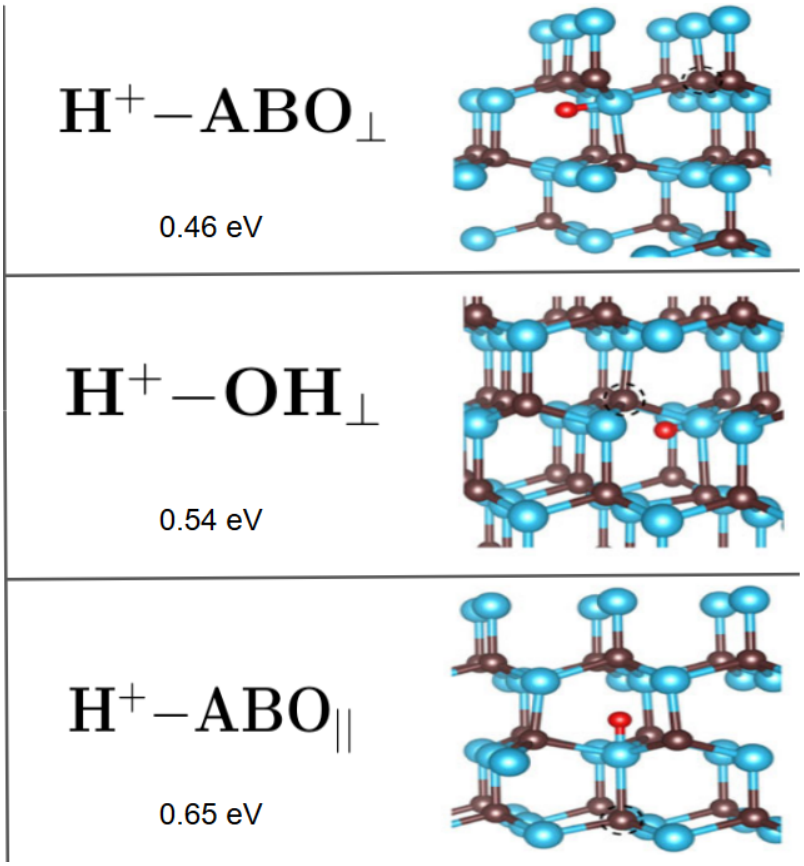

Figure 1.6: Higher energy metastable configurations for Mu^+. States $H^+-ABO_{||}$ $H^+-ABO_{\perp}$ were obtained by placing hydrogen in the anti-bonding oxygen sites, see Fig 1.4. The $H^+-OH_{\perp}$ is a result of placing hydrogen in a bond center site. The parallel and perpendicular designation correspond to the orientation of the O−H bond relative to the c axis of the crystal. The energy values depicted are the formation energies of each state. Adapted from [MVV+17]

In the bond center sites, the H^+ ion pushes the Be atom away due to Coulomb forces. This results in a OH bond. The ground state, $H^+-OH_{||}$, leaves the Be nuclei to form a new bond with another oxygen atom of the lattice (represented by the star in Fig. 1.5). For the perpendicular case ($H^+-OH_{\perp}$) there is some displacement of the H^+ and Be atoms due to the repulsive force acting between them. However the original Be−O bound persists during the relaxation of the lattice.

In *ab-initio* calculations the introduction of hydrogen in the anti-bonding sites was found to be much more stable when compared to the bond center sites. Unlike the previous site, no Be−O bonds were broken and their configuration remained pretty much the same until total relaxation of the lattice.

For H^0 the predicted ground state is depicted in Fig. 1.7. The higher energy metastable configurations corresponding to excited states are shown in Fig. 1.8.

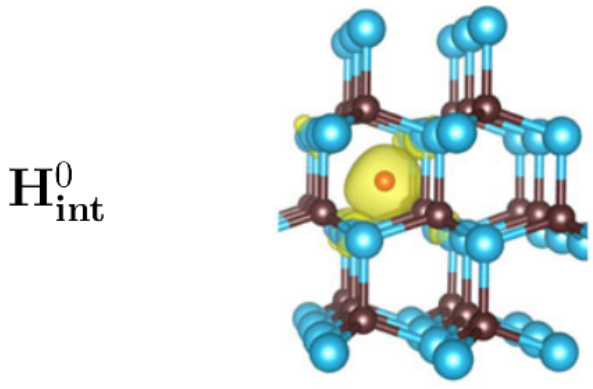

Figure 1.7: Predicted ground state configuration for H^0. The Hydrogen atom is the little red sphere. The yellow spots represent the spin density isosurface. Adapted from [MVV+17]

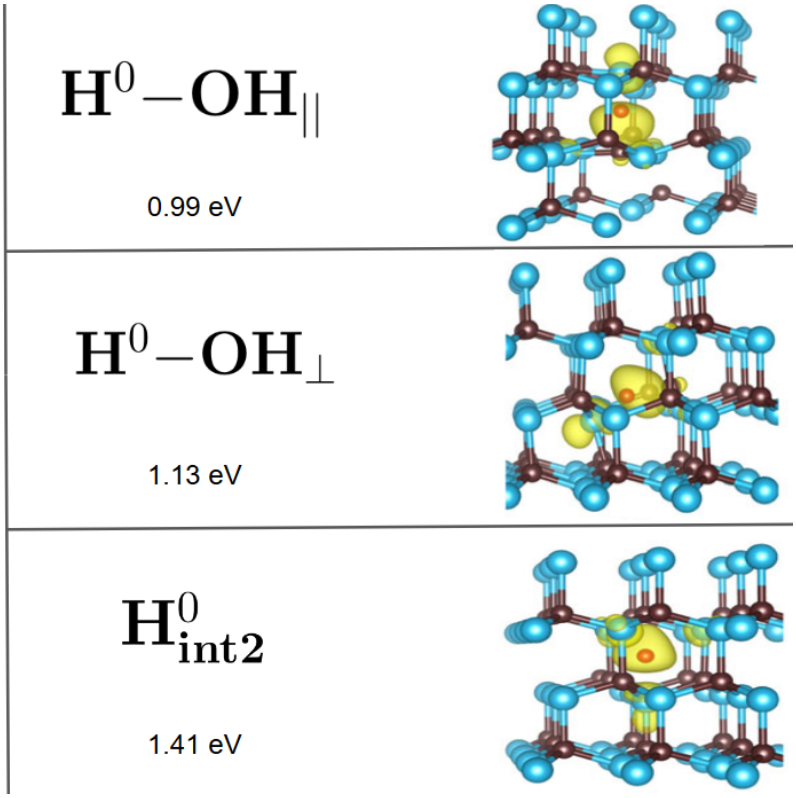

Figure 1.8: Higher energy metastable configurations for H^0. Analogously to the previous case, states $H^0-OH_{||}$ and $H^0-OH_{\perp}$ correspond to the adopted configuration for hydrogen placed at the bond center site. State H^0_{int2} was obtained by placing hydrogen in the anti-bonding oxygen sites, stabilizing at an interstitial position. The parallel and perpendicular designation correspond the orientation of the O−H bond relative to the c axis of the crystal. The energy values depicted are the formation energies of each state. Adapted from [MVV+17]

The presence of hydrogen in Fig. 1.7 is located in a highly symmetric position, the center of the hexagonal, interstitial site of the lattice. In this position, H^0 keeps a maximum distance of the Be nuclei, about 1.67 $\mathring{A}$, hence minimizing energy. Besides this, H^0 also adopted other stable configurations after neutralizing the bond center H^+ states, which correspond to $H^0-OH_{\perp}$ and $H^0-OH_{||}$. The other higher energy metastable configuration, H^0_{int2} was obtained by placing the hydrogen atom in the $ABO_{||}$ site. The *ab-initio* calculations allowed to extract the hyperfine parameter of the neutral hydrogen configuration. The hyperfine constant conveys the electronic density at the nucleus. This will be further explained in the next chapter. The computed isotropic and dipolar hyperfine constants are expressed in table 1.1. As expected, the most isotropic states are the interstitial ones, where the dipolar con-

stant is very small compared to their bounded counterparts. Figure 1.9 represents the band diagram for the different protium states.

State	A_{iso}	D
H^0_{int}	1460	-
$H^0-OH_{\|\|}$	693	60
$H^0-OH_{\perp}$	655	56
H^0_{int2}	1307	5

Table 1.1: The isotropic and dipolar hyperfine constants from the neutral hydrogen configurations

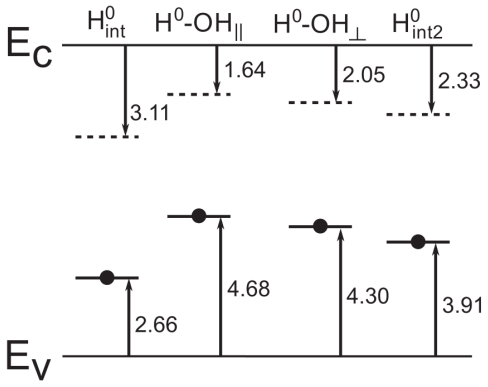

Figure 1.9: Energy levels for the different muonium states. The calculated band gap was of 10.58 eV. Dashed and solid lines correspond to the donor and acceptor levels for each different state. Adapted from [MVV$^+$17]

Considering these energy levels for the H^+ states, and knowing that the calculated band gap was of 10.58 eV, it is now possible to inspect the transition between the positively and neutrally charged configurations.

As an example, lets consider the H^+_{int} / H^0_{int} case. The H^0_{int} state has a 2.66 eV level above the valence band. The ground state energy for H^0 was inspected to be approximately 4.33 eV. In this example, H^0_{int} happens to be the ground state which means no formation energy must be added. Since the formation energy and the Fermi level are linearly proportional, one can plot the following graph (Fig. 1.10).

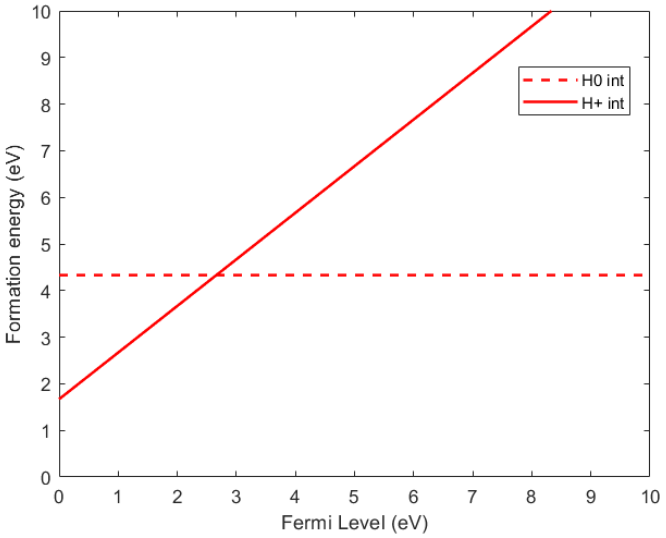

Figure 1.10: Plot for a single transition between the H^+ and H^0 states. Note the intersection for $x = 2.66$ eV, $y = 4.33$ eV.

This procedure is repeated for the other states and the following plot is the final result. (Fig. 1.11).

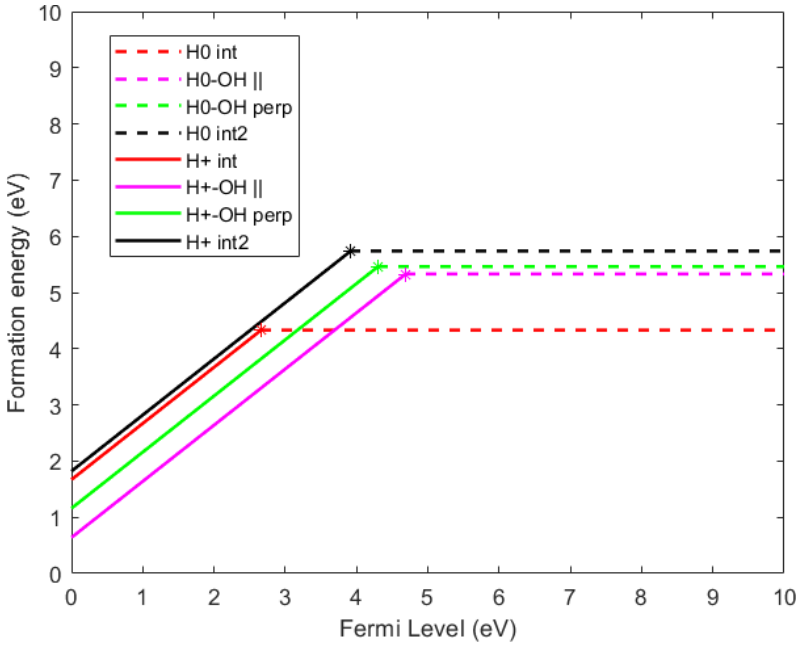

Figure 1.11: Formation energy plot of all the states of $H^{0/+}$ as a function of the Fermi-level position in the gap. Note that the irrelevant parts of the plot (non stable states) were trimmed.

As expected, the most stable configuration is $H^{+}-OH_{||}$, seeing as it is the ground state. However, as the Fermi level starts to increase, neutral hydrogen configurations are preferred.

2

Experimental methods

2.1 The μSR technique

> "μSR stands for Muon Spin Relaxation, Rotation, Resonance, Research or what have you."
>
> Yamazaki, Nagamine, Crowe, and Brewer, 1974

2.1.1 General overview

Positive muon spectroscopy[1] is a local probe technique used to extract local information on the properties of materials. It has applications in the study of magnetic, superconducting semi-conducting and insulating materials [LBP13] [MBC$^+$13] [CLL$^+$13].

The procedure itself consists of implanting spin polarized muons into the sample, in which they will lodge until their life ends. Their kinetic energy starts typically at 4 Mev, which will start to decrease due to ionization effects. However, it is important to underline that every process the muon undertakes before stopping in the crystal lattice of the material does not affect its spin, which means the original polarization is mostly kept until the muon reaches its final stopping site [Uem98]. Here, its spin is constantly affected by local magnetic fields and spin dynamics. These can and often will change the original polarization of the muon. In non magnetic materials (which are the object of this study) this process is called **relaxation**.

[1] from now on the positive/anti muon will be referred to as muon

One thing left out of this description was the fact that during the experiment a constant external magnetic field is applied. This will cause the spin of the muon to precess (unless a longitudinal magnetic field experiment is taking place) [Vil07]. Due to the previously mentioned relaxation effects, the behavior of the muon evolves over time. By monitoring the changes in amplitude, phase, frequency and in the relaxation parameters of the μSR signal, it is possible to reach conclusions about a whole plethora of different effects the local fields have on the particle and ultimately get a better grasp as to how the hydrogen impurities are affected by their environment.

2.1.2 Positron detection

As a matter of fact, the muon is not directly measured, instead, its presence is inferred by detecting its footprint, the positron. During its whole life cycle, the muon never really leaves the sample, it undergoes the following decay:

$$\mu^+ \longrightarrow e^+ + \nu_e + \bar{\nu_\mu} \tag{2.1}$$

This particle follows the typical exponential decay and its average lifetime is approximately 2.2 μs. The energy with which the positron is emitted can vary from 0 up to 52.3 MeV [Alb17]. Due to the weak interaction nature of this process, parity is not conserved and the positron will be preferably emitted in the direction of the muon spin. The word preferably is not chosen lightly. It is a key word that encompasses an important detail: not all positrons are emitted in the direction of the muon spin; it is a statistical process. The higher the energy of the positrons, the higher their probability of being emitted in the direction of the muon spin. In practice, there is no energy discrimination and therefore the average angular distribution is observed (Fig. 2.1 orange line).

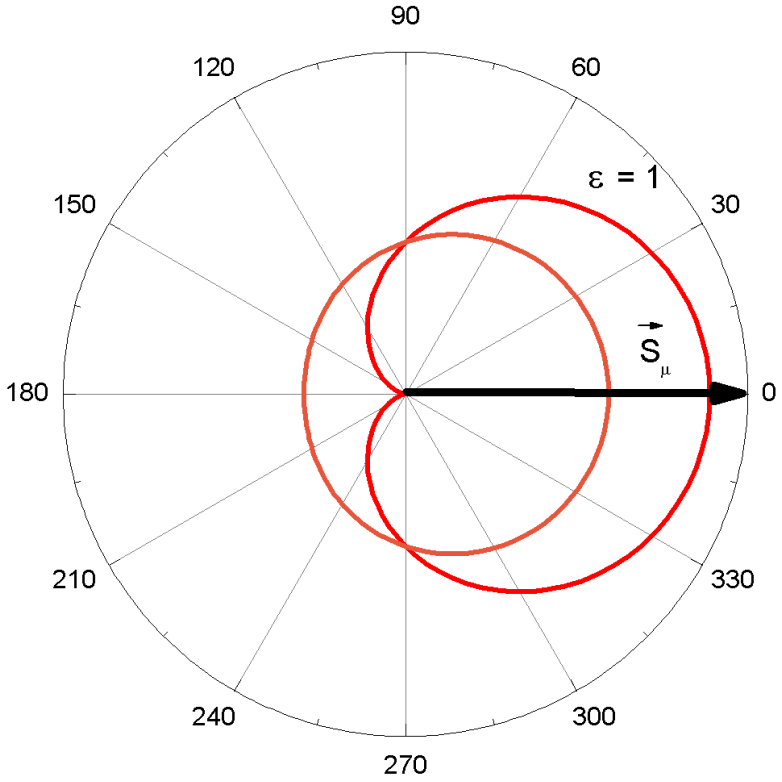

Figure 2.1: Angular distribution of positron emission. The red curve indicates the higher energy positrons. The orange line represents the integration over all energies. The arrow is the initial muon spin polarization.

2.2 A tale of two particles

2.2.1 Muon

As it was discussed above, muons can be used as a very sensitive probe for local magnetic fields. However in the case of insulators/semiconductors, muons are used to model the electronic structure of hydrogen impurities inside the sample. This is viable because muons and hydrogen ions have some very similar properties (see tables 2.1 and 2.2). In fact, it is often said that the muon is a lighter, pseudo-isotope of hydrogen.

	μ^+	H^+
Charge/e	1	1
Mass/m_p	0.1126	1
Spin/$\hbar$	1/2	1/2
Gyromagnetic ratio/γ_p	3.17	1
Decay time (μs)	2.197	stable

Table 2.1: Muon and proton properties adapted from [Vil07]

In μSR experiments, often a transverse (perpendicular to the initial spin polarization) magnetic field is applied. Consequently, the spin of the muon precesses at the Larmor frequency, ω_L (Fig. 2.2).

$$\omega_L = \gamma_\mu B \tag{2.2}$$

Where γ_μ being the gyromagnetic ratio of the muon $\gamma_\mu = 2\pi \times 135.53$ MHz/T.

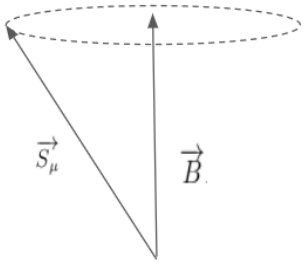

Figure 2.2: Spin precession of the muon caused by a transverse magnetic field.

2.2.2 Muonium

Implanted muons can capture an electron and thermalize as muonium which is comparable to the hydrogen atom [Uem98]. From a purely condensed matter physics point of view the muon and muonium can be seen respectively as a light proton (H^+) and a light protium[2] (H).

[2]The most stable Hydrogen isotope

	Mu	H
Reduced mass (m_e)	0.995	0.999
Binding energy (eV)	13.54	13.60
Hyperfine parameter MHz	4463.3	1420.4
Atomic radius (Å)	0.532	0.529

Table 2.2: Muonium and protium properties for ground state adapted from [Vil07]

In muonium the electronic and muonic spins are coupled by the hyperfine interaction. In a first approximation[3] this may be described by an isotropic Fermi contact interaction of the form $A\,\vec{S_\mu}\cdot\vec{S_e}$. Here, A is the hyperfine interaction constant which is defined by equation 2.3. For muonium in vacuum, $A = 4463.3$ MHz [Vil07].

$$A = \frac{\omega_0}{2\pi} = -\frac{2}{3h}\mu_0 g_\mu \mu_\mu g_e \mu_B |\Psi(r=0)|^2 \tag{2.3}$$

Where,

- ω_0 is the angular frequency of the Fermi contact interaction
- S_μ, S_e the spin operators of the muon and the electron respectively.
- g_μ, g_e is the gyromagnetic factor of the muon and the electron respectively
- μ_μ the muon magneton $\mu_\mu = \frac{e\hbar}{2m_\mu}$
- the gyromagnetic factor of the electron
- μ_B the Bohr magneton $\mu_B = \frac{e\hbar}{2m_e}$

[3]This may not always be the case although during the experiment anisotropic muonium could not be observed, nonetheless this will be discussed further ahead.

In the presence of an external magnetic field B, the spin Hamiltonian becomes:

$$H = \frac{\hbar}{4}\omega_0 S_\mu \cdot S_e - \frac{\hbar}{2}\omega_\mu S_{\mu,z} + \frac{\hbar}{2}\omega_e S_{e,z} \tag{2.4}$$

$$\omega_\mu = 2\pi\gamma_\mu B \tag{2.5}$$

$$\omega_e = 2\pi\gamma_e B \tag{2.6}$$

- $\omega_\mu,\ \omega_e$ are the precession angular frequencies of the isolated muon and electron respectively.
- γ_μ is the gyromagnetic ratio of the muon $\gamma_\mu = \frac{g_\mu \mu_\mu}{h} = 135.53\text{MHz/T}$
- γ_e is the gyromagnetic ratio of the electron $\gamma_e = \frac{g_e \mu_e}{h} = 28024.21$ MHz/T

It also will be convenient to define the following quantities:

$$\omega_\pm = \frac{\omega_e \pm \omega_\mu}{2} \tag{2.7}$$

$$x = \frac{2\omega_+}{\omega_0} = \frac{B}{B_0} \tag{2.8}$$

$$B_0 = \frac{\hbar\omega_0}{g_\mu\mu_\mu - g_e\mu_B} \tag{2.9}$$

B_0 is the magnetic field corresponding to the hyperfine interaction in vacuum and has a value of 0.1585 T. Using $|m_\mu\ m_e\rangle$ as the basis for the spin space, one can solve equation 2.4 and thus find the eigenvalues [Pat88][Vil07][Per11]. The results are exposed in the table 2.3 .

Eigenstate	Eigenvector	$E_n/\ \hbar$
$\|1\rangle$	$\|++\rangle$	$\frac{\omega_0}{4}+\omega_-$
$\|2\rangle$	$\alpha\|+-\rangle+\beta\|-+\rangle$	$\frac{-\omega_0}{4}+\frac{\omega_0}{2}\left[x^2+1\right]^{1/2}$
$\|3\rangle$	$\|--\rangle$	$\frac{\omega_0}{4}-\omega_-$
$\|4\rangle$	$\alpha\|-+\rangle-\beta\|+-\rangle$	$\frac{-\omega_0}{4}-\frac{\omega_0}{2}\left[x^2+1\right]^{1/2}$

Table 2.3: The general solution of the Hamiltonian.

$$|\alpha|^2=\frac{1}{2}\left(1+\frac{x}{\left[1+x^2\right]^{1/2}}\right) \tag{2.10}$$

$$|\beta|^2=\frac{1}{2}\left(1-\frac{x}{\left[1+x^2\right]^{1/2}}\right) \tag{2.11}$$

In the low field region a triplet and a singlet state arise. It is now more convenient to change the basis of the spin space to that of the total spin, F, and its projection on the z axis, m_F. In zero field, table 2.3 can be written as:

Eigenstate $\|F\ m_F\rangle$	Eigenvector	$E_n/\ \hbar$
$\|1\ 1\rangle$	$\|++\rangle$	$\frac{\omega_0}{4}$
$\|1\ 0\rangle$	$\frac{\sqrt{2}}{2}\|+-\rangle+\frac{\sqrt{2}}{2}\|-+\rangle$	$\frac{\omega_0}{4}$
$\|1$ -1$\rangle$	$\|--\rangle$	$\frac{\omega_0}{4}$
$\|0\ 0\rangle$	$\frac{\sqrt{2}}{2}\|-+\rangle-\frac{\sqrt{2}}{2}\|+-\rangle$	$\frac{-3\omega_0}{4}$

Table 2.4: The solution of the Hamiltonian for the zero field limit.

These tables can be summarized in the Breit-Rabi energy diagram (Fig. 2.3).

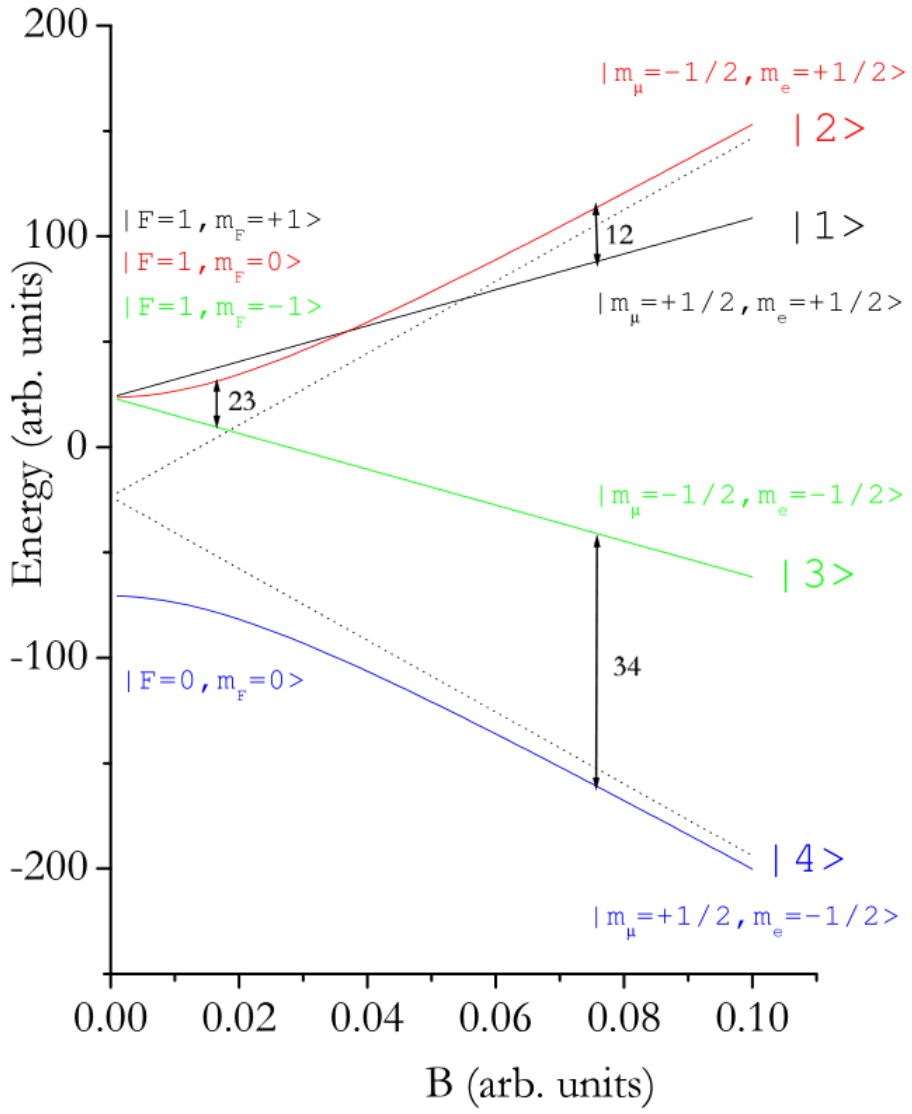

Figure 2.3: The Breit-Rabi energy diagram. This figure displays the hyperfine interaction energy with respect to the x parameter defined in equation 2.8 Note that a fake value of $\frac{\omega_+}{\omega_-}$ was used in order to bring out some important details of the diagram. Furthermore, the dashed lines correspond to the asymptotic limits for the high field energy states. For low fields, the singlet and triplet energy states are easily observable. For high fields, the Zeeman term starts dominating the interactions and the hyperfine component becomes negligible, originating two simple energy levels separated by the Larmor energy. Extracted from [Vil07]

Muonium will oscillate between states. The transitions for low fields are governed by the following selection rules [Sch85]:

$$\Delta F = 0,\, 1$$

$$\Delta m_F = 1$$

By applying these restrictions the following transitions arise:

nm	a_{nm}	$2\pi\nu_{nm}$
1 2	$\frac{\lvert\beta\rvert^2}{2}$	$\frac{\omega_0}{2} + \omega_- - \frac{\omega_0}{2}\left[1+x^2\right]^{1/2}$
3 4	$\frac{\lvert\beta\rvert^2}{2}$	$\frac{\omega_0}{2} - \omega_- + \frac{\omega_0}{2}\left[1+x^2\right]^{1/2}$
1 4	$\frac{\lvert\alpha\rvert^2}{2}$	$\frac{\omega_0}{2} + \omega_- + \frac{\omega_0}{2}\left[1+x^2\right]^{1/2}$
2 3	$\frac{\lvert\alpha\rvert^2}{2}$	$\frac{-\omega_0}{2} + \omega_- + \frac{\omega_0}{2}\left[1+x^2\right]^{1/2}$

Table 2.5: The precession angular frequencies for isotropic muonium as a consequence of the low field selection rules.

These oscillation frequencies are the parameters that can be directly extracted from experimental data. The low field transitions look like this:

nm	a_{nm}	$2\pi\nu_{nm}$
1 2	$\frac{\lvert\beta\rvert^2}{2}$	ω_-
3 4	$\frac{\lvert\beta\rvert^2}{2}$	$\omega_0 - \omega_-$
1 4	$\frac{\lvert\alpha\rvert^2}{2}$	$\omega_0 + \omega_-$
2 3	$\frac{\lvert\alpha\rvert^2}{2}$	ω_-

Table 2.6: The solution of the Hamiltonian from Eq. 2.4 for the low field limit, $B << B_0$.

Transverse magnetic field measurements were mainly done with what are being considered as low fields ($B << B_0$). The transitions that should be observed are therefore the ones present in table 2.6. However, in practice the only observable transitions are 1 2 and 2 3 due to the others having an extremely high precession frequency. Note that for a 10 G magnetic field, $\nu_{12} = \nu_{23} \approx 13.94$ MHz whereas $\nu_{14} = \nu_{34} \approx 4463.3$ MHz. Regarding the former, whether or not these frequencies are observable will depend on the detectors themselves, more specifically their frequency resolution. This will be discussed with further detail in the following section.

In general, the precession frequency of the transitions with respect to the magnetic field evolves like so (Fig. 2.4).

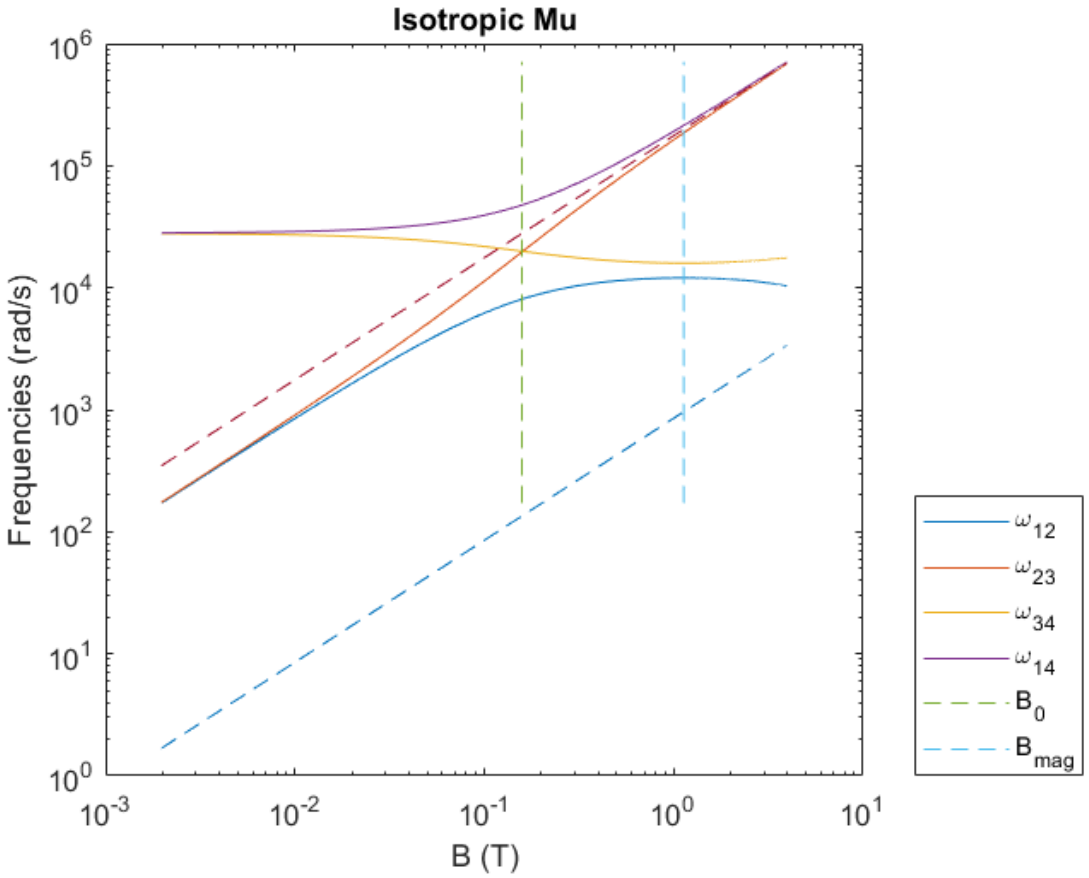

Figure 2.4: The precession frequency of the different transitions with respect to the applied transverse magnetic field for isotropic muonium. B_0 is the magnetic field corresponding to the hyperfine interaction in vacuum (0.1585 T) and B_{mag} the field at which the 1 2 and 3 4 transitions are approximately equal and independent of the applied field. The diagonal dashed lines correspond to the electron (red) and muon (blue) precession frequencies. Extracted from [Vil07]

.

As the transverse magnetic field increases, the amplitude of the signal will also change as depicted in figure 2.5. The amplitude of transitions ν_{23} and ν_{14} drops to zero at approximately 1 T. The signal is therefore comprised of amplitudes ν_{12} and ν_{34}.

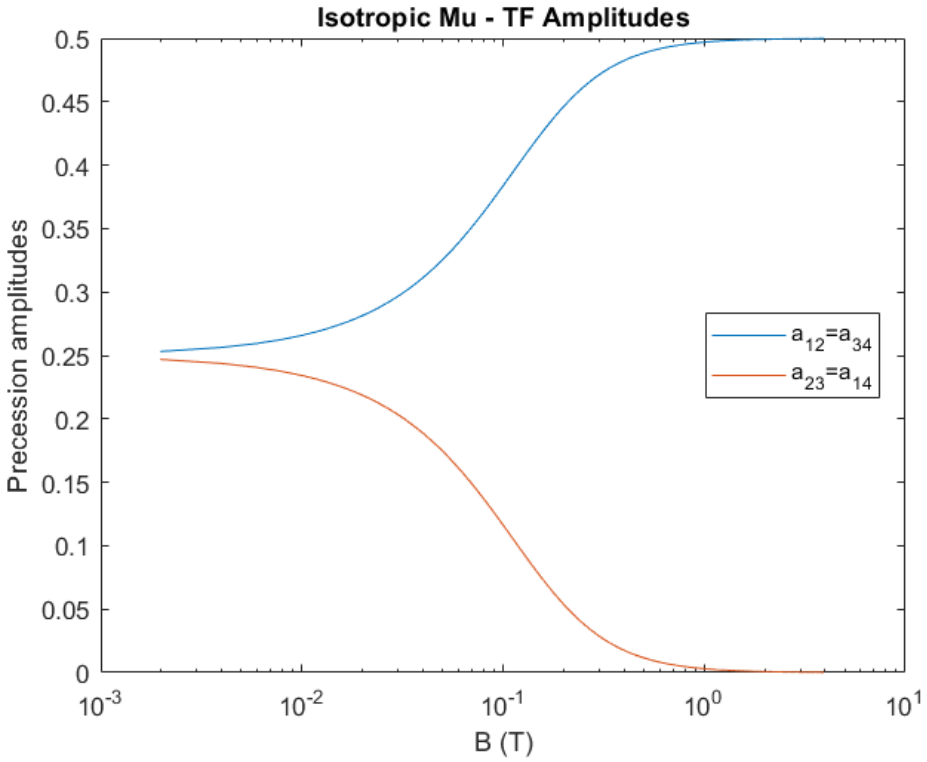

Figure 2.5: The amplitude of the different transitions with respect to the increase of the transverse magnetic field. Extracted from [Vil07]

.

2.3 The Muon beam

Muons are produced in the upper atmosphere as a result of various reactions with cosmic rays. However, in scientific experiments, muon beams are artificially created with particle accelerators. This process envelops several steps. Figure 2.6 depicts the scheme of the ISIS (United Kingdom) spallation source where most of the experimental work discussed on this essay takes place. Here, protons go through the linear accelerator ("Linac") to the synchrotron where they are accelerated even further. Then, they are redirected to one of the two tungsten spallation targets in order to produce neutrons (Target 1 and Target 2 in Fig. 2.6).

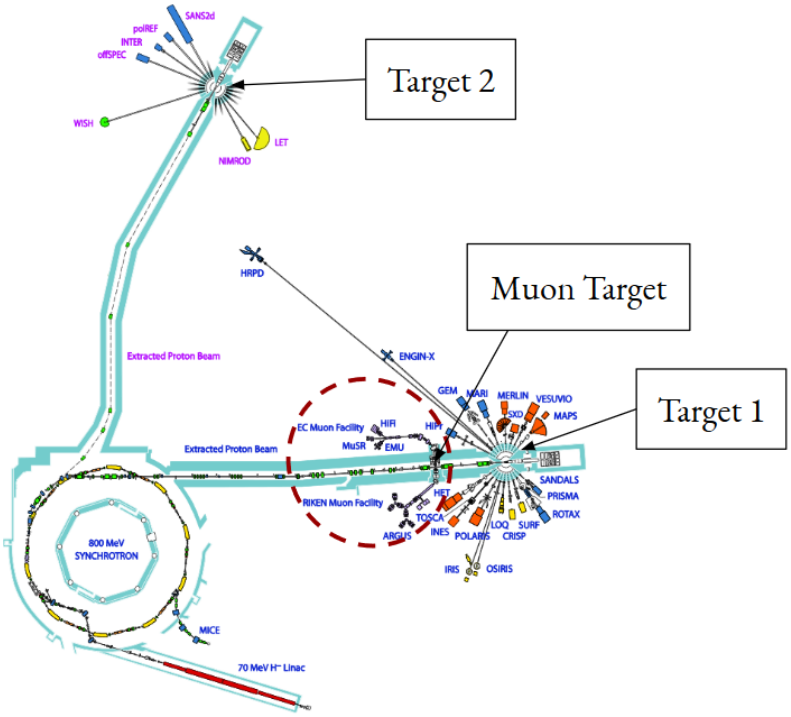

Figure 2.6: Scheme representing the ISIS facility with the respective spallation targets. Within the red dashed lines are the muon instruments, where the experimental work presented in this dissertation took place, more specifically at the HiFi instrument. Image adapted from [Hil14b].

The 800 MeV proton beam directed at Target 1 crosses an additional target, usually graphite (Fig. 2.7) which does not compromise the luminosity of the beam since it only uses 4% of the beam. In this graphite target pions are produced through the nuclear reaction:

$$p + p \longrightarrow \pi^+ + p + n \tag{2.12}$$

Pions are unstable particles with a mean lifetime of 26 ns and zero spin. Eventually they will decay into a muon neutrino and a positive muon through the weak interaction.

$$\pi^+ \longrightarrow \mu^+ + \nu_\mu \tag{2.13}$$

The muons are then extracted from the decaying pions on the surface of the graphite target.

Figure 2.7: Graphite target used at ISIS facilities in England with dimensions $50 \times 50 \times 7$ mm.

In fact, the neutrino has a negative helicity which basically means that its linear momentum and spin orientation are anti-parallel. The conservation of linear and angular momentum dictates that the muons must mirror this behavior. This is the procedure that ensures the production of nearly 100 % spin polarized muon beams used in muon spectroscopy [Ren14].

As of now (May 2018) there are only four facilities in the world that perform muon spectroscopy experiments. These are ISIS (United Kingdom), TRIUMF (Canada), PSI (Switzerland) and J-Park (Japan). The nature of the beam varies, it can be continuous like in TRIUMF or PSI or pulsed like in ISIS and J-Park [Alb17].

The data discussed in this essay were basically collected in the HiFi instrument at ISIS (Fig. 2.8). Some existing data taken by Vilao, et al at the General Purpose Surface-Muon Instrument (GPS) at PSI (Fig. 2.9) will also be discussed in order to complement the ISIS data of this work (regarding the neutral configuration, Mu^0).

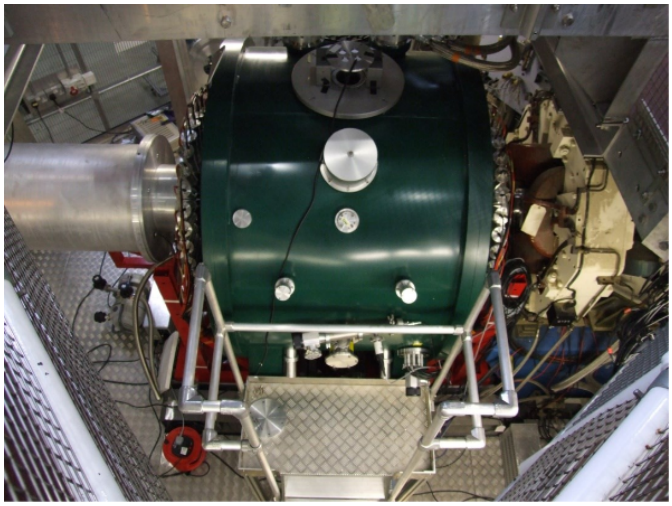

Figure 2.8: The HiFi instrument at the ISIS facility in the United Kingdom.

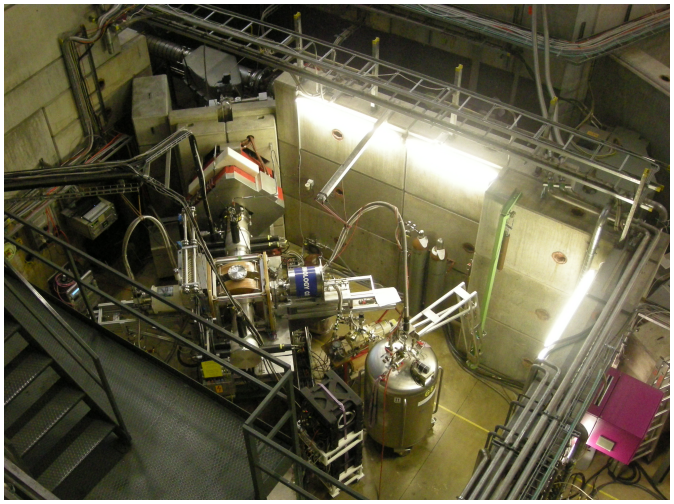

Figure 2.9: The GPS instrument at the PSI muon facility in Switzerland.

With a continuous muon beam like the one in PSI, muons arrive intermittently to the material, each starting a clock that will only stop when the respective positron is detected. These continuous muon sources allow to push the time resolution to the maximum supported by the detectors. However, seeing as there is a low incident muon arrival rate, false positive readings become very significant, which means that the measurements will be accompanied by a relatively large background. As the time window stretches, the muons decay, fewer counts are registered and therefore the background becomes increasingly relevant. This imposes a strong limitation regarding the maximum time window for continuous muon sources. In pulsed muon

beams a burst of muons reaches the sample at approximately the same time. A clock starts at t = 0 and registers the time passed whenever a positron is detected. This time interval is sent to a processing unit that groups all of the events [Blu99]. Due to a high muon arrival rate, these sources do not suffer from the same limitations to the maximum time window and are therefore adequate to probe processes that can encompass up to $10 - 15$ muon lifetimes. However the time resolution is here much affected by the temporal width of the muon pulse. In ISIS this is ~ 70 ns which limits the maximum observable frequency to ~ 14 MHz. Figure 2.10 illustrates these differences.

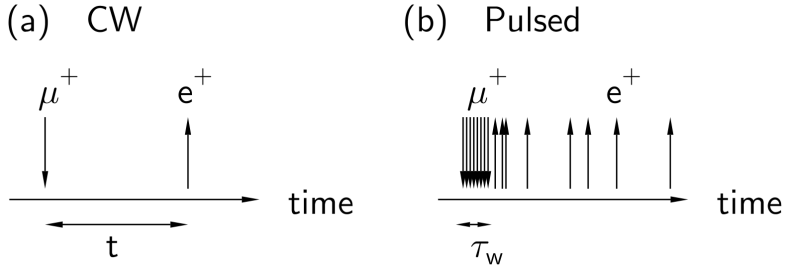

Figure 2.10: The continuous wave and pulsed muon beams. Notice how the burst of muons has a finite length, τ_W, from [Blu99]

The following figure (Fig. 2.11) will summarize the pulsed muon beam, the event timing mechanism and the magnetic field induced precession.

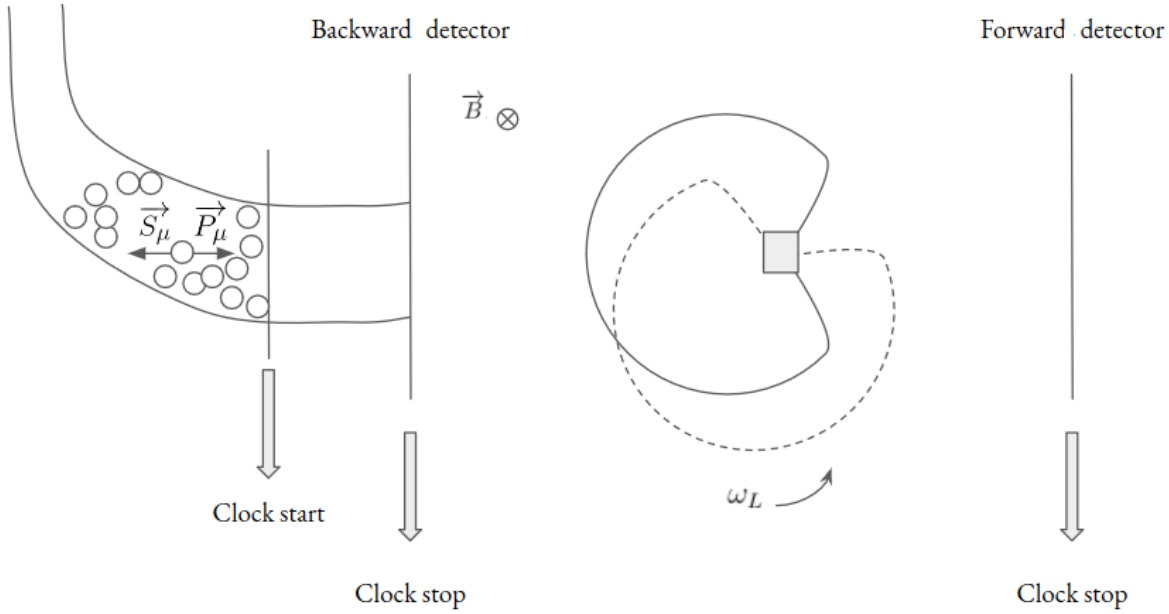

Figure 2.11: Diagram of the start stop clock mechanism of the pulsed muon beam. For clarity purposes only the angular distribution of the higher energy positrons was represented. Different time intervals for positron emission can be seen at $t = 0$ and at $t \neq 0$ (dashed line). Notice that the orientation of positron emission pattern varies with time, accompanying the precession of the muon spin in the presence of the external magnetic field.

When analyzing data the positron detectors are grouped according to their geometry. By placing two opposite groups of detectors it is possible to define an asymmetry function like so:

$$A(t) = \frac{N_B - \alpha N_F}{N_B + \alpha N_F} \tag{2.14}$$

Where

- N_B and N_F are the number of counts on the backward and forward detectors.
- α is the correction parameter which originates from an imbalance regarding positron detection. This can arise either from geometrical imbalance on the position of the detectors or from differences in the efficiency of the detectors.

If precession is involved like in Fig. 2.11 it is expected that the maximum number of counts for one detector group corresponds to the minimum on the opposite side.

Figure 2.12 is an example of some raw data from a muon spectroscopy experiment that illustrates this principle.

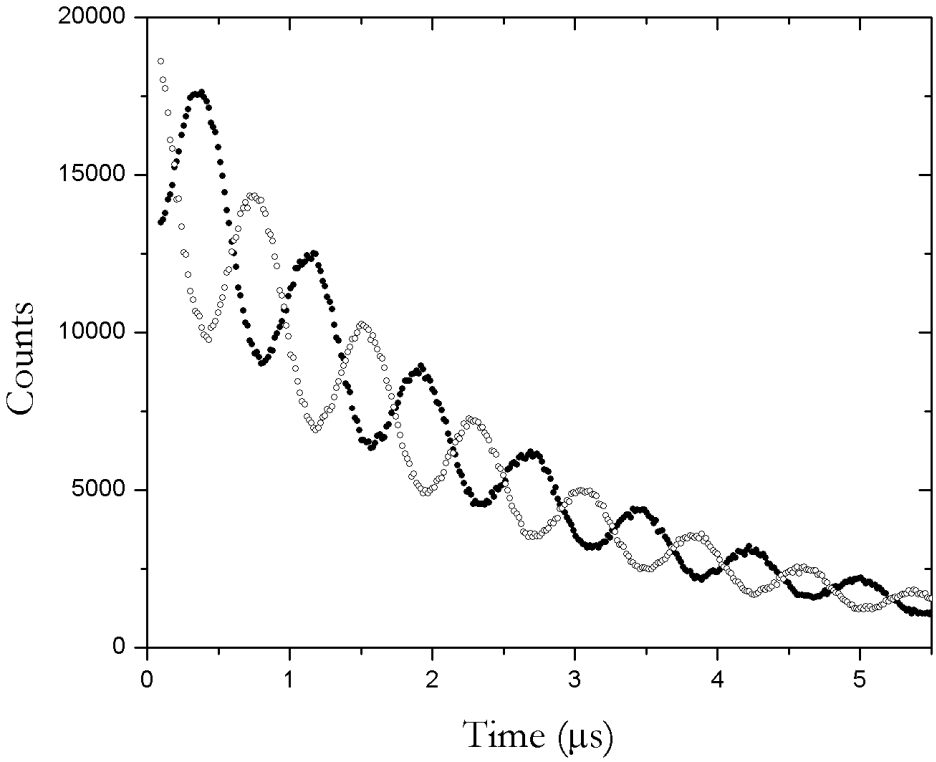

Figure 2.12: Data from a μSR experiment. In gray are represented the counts from forwards detector group and in black the counts from the backwards detector group. The observed pattern is a consequence of the precession of the muons.

The α parameter has a significant impact on the data and must be accounted for. In order to understand how the calibration of the detectors can affect data, the illustrations below will showcase a transverse μSR signal before and after correcting the previously mentioned α parameter.

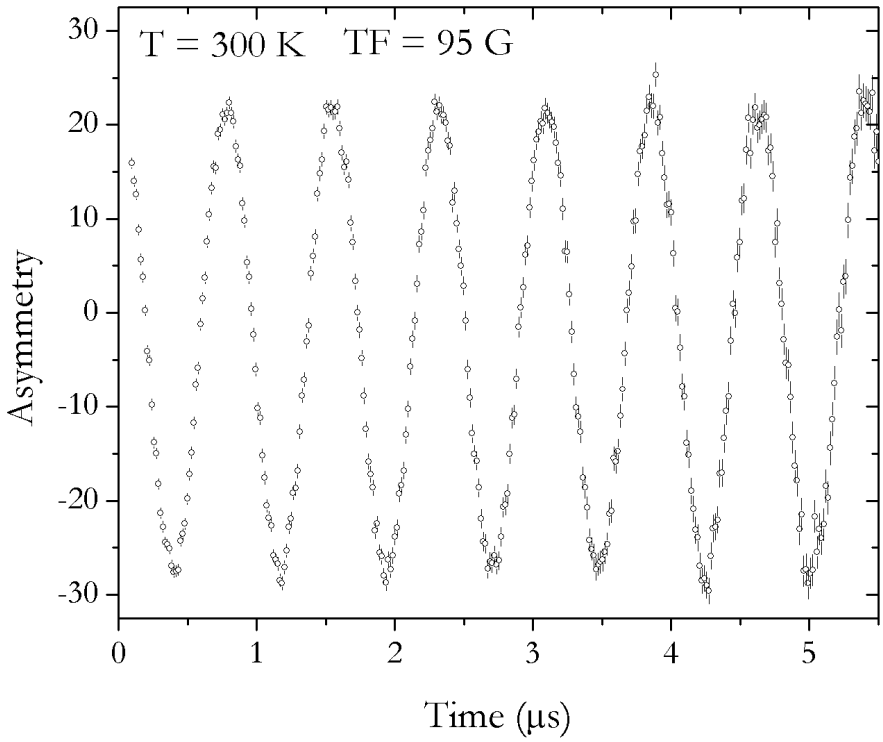

Figure 2.13: Silver sample asymmetry function before calibration, data collected at ISIS, UK from an October 2017 experiment.

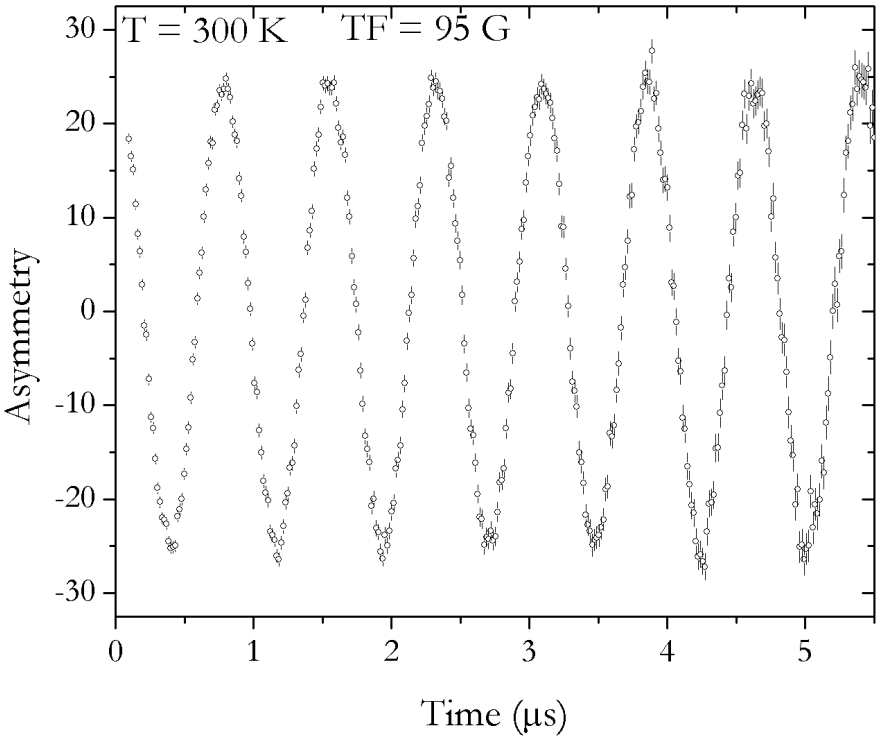

Figure 2.14: Silver sample asymmetry function after calibration, data collected at ISIS, UK from an October 2017 experiment.

Extracting α is done by simply enforcing the oscillation to be around 0%, in this particular case, $\alpha = 0.94972$.

Muons in silver do not exhibit any significant relaxation and simply precess with the Larmor frequency (see Eq. 2.2) when a transverse magnetic field is applied. Consequently, silver can be used to extract the maximum instrumental asymmetry (for transverse fields). This should, in theory, be around 33% which is a consequence of the weak interaction (see Fig. 2.1). However due to the detectors having a finite length and not being 100% efficient, this is usually reduced to somewhere around 25% [Hil14a] [Alb17].

2.4 Longitudinal magnetic field

Unless zero field measurements are being taken, there is usually a magnetic field involved in μSR experiments. This can either be perpendicular (transverse) or parallel (longitudinal) to the initial muon spin polarization. All that was discussed up until this point was the transverse field case. However longitudinal field measurements provide valuable information as well.

When a longitudinal magnetic field is applied, all the muons states become eigenstates because they are aligned with the field. In comparison with the transverse field, this technique facilitates the detection of the relaxation of the muon spin. This relaxation can be the result of static effects such as local magnetic field distributions, or dynamic effects such as the interaction with charge carriers. The longitudinal field technique is therefore sometimes designated by muon spin relaxation. A single longitudinal field spectrum will look like Fig. 2.15

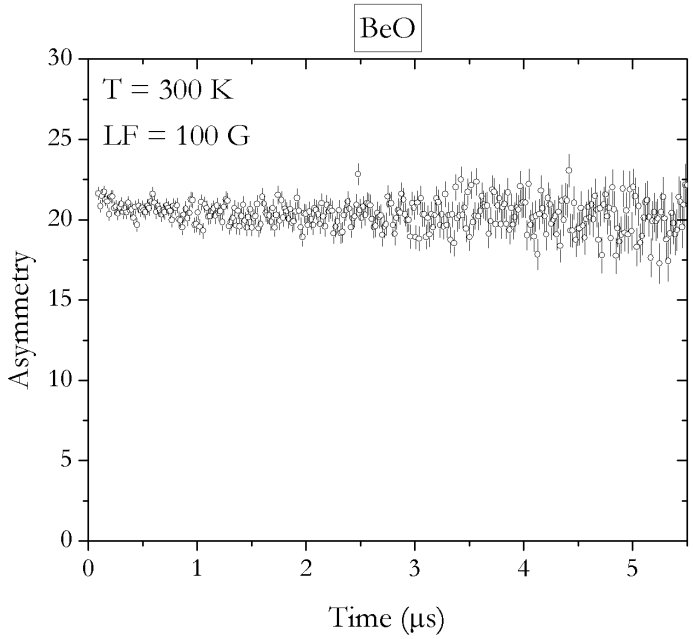

Figure 2.15: Beryllium oxide asymmetry in a 100 G longidtuinal field at a temperature of 300 K, data collected at ISIS, UK from an October 2017 experiment.

Besides muons, there is the formation of muonium. Here it is important to remember that the muons are initially polarized, but the electrons are not, their spin can either be parallel or anti-parallel to that of the muon. When taking into account the longitudinal magnetic field, this means that when it is formed, muonium has a 50% chance of being in an eigenstate. The other half oscillates between states $|2\rangle$ and $|4\rangle$ (see table 2.3) with an angular frequency of $\omega_{24} = \omega_0 \left[1 + x^2\right]^{1/2}$.

As the longitudinal field starts to increase towards the Paschen-Back *régime*, the contribution of the hyperfine parameter to the Hamiltonian (Eq. 2.4) will eventually become negligible (compared to the Zeeman terms). This means that, in practice $|m_\mu\rangle$ and $|m_e\rangle$ become decoupled and align with the longitudinal field. Thus total polarization is achieved.

The polarization of muonium in the direction of the longitudinal field can be approximately described by the function [4]:

$$p_z = \frac{1}{2}\left[1 + \frac{x^2}{1+x^2}\right] \tag{2.15}$$

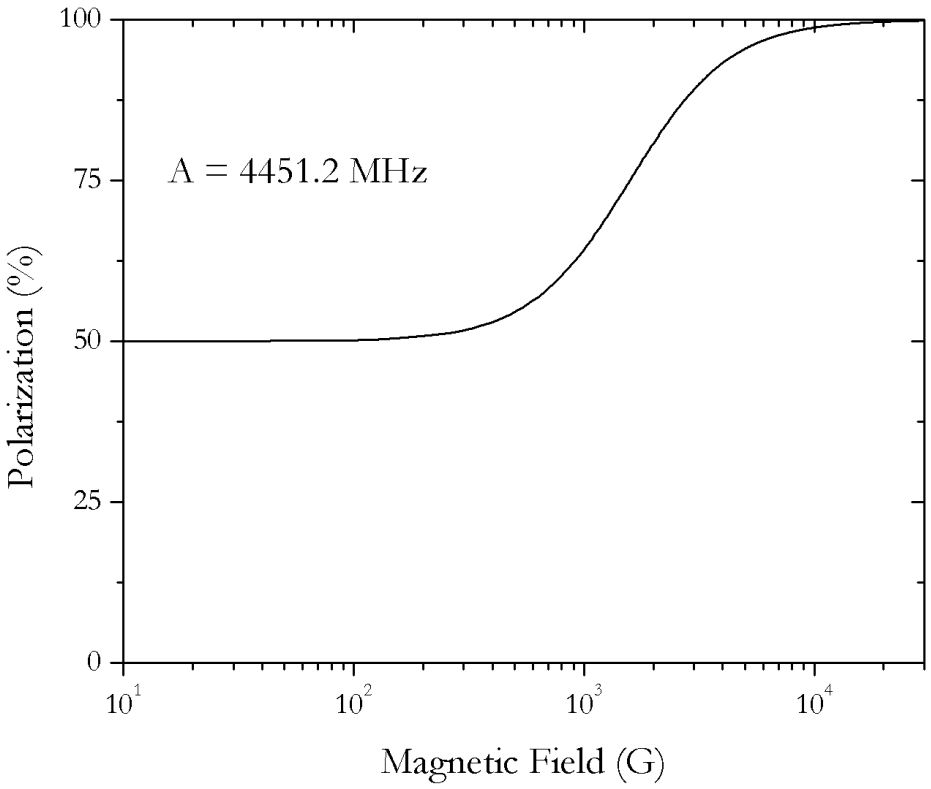

Figure 2.16: The repolarization curve for a hyperfine constant of A = 4451.2 MHz which corresponds to muonium in the $H^0_{textint}$ state, the predicted ground state in *ab-initio* calculations (see section 1.3).

By sweeping the longitudinal field it is possible to estimate the strength of the hyperfine interaction as well as the muonium anisotropy by fitting the previous function to a repolarization curve (Fig. 2.16).

[4]Remember, $x = \frac{2\omega_+}{\omega_0} = \frac{B}{B_0}$

3

Characterization of the local magnetic fields

One of the main difficulties of this work was determining the site occupied by the muon particle. The location of the muon can be tracked by studying its relaxation. This relaxation can be estimated with the help of some theoretical framework presented on the following section.

Another way of estimating the location of the particle rests on a technique called the quadrupole avoided level-crossing which composes the second and third part of this chapter.

3.1 Muon relaxation in the Van Vleck limit

In this section some theoretical framework is presented in an attempt at estimating the relaxation rate of the muon particle in a given stopping site. It is important to understand the focus here is on the muon particle alone, no muonium is being considered. This will be particularly relevant when discussing the experimental data relative to the positively charged muon. The estimate of the relaxation of the muon is done in the limit where only the dipolar interaction between the muon and neighboring nuclei is considered.

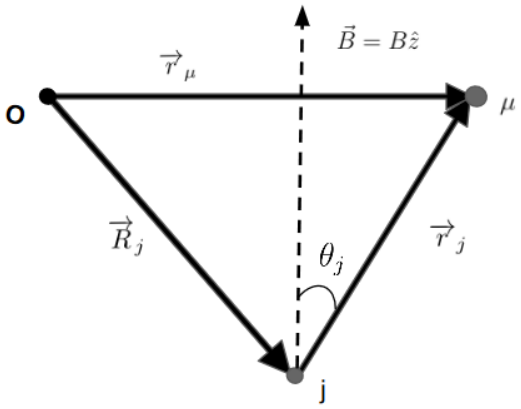

Figure 3.1: The vector diagram of the magnetic dipole interaction with an applied magnetic field $\vec{B}$ relative to an origin, O. The distance between the muon (in the r_μ position) and an arbitrary nucleus j (in the $\vec{R}_j$ position) is given by $\vec{r_j} = \vec{r_\mu} - \vec{R}_j$.

The hamiltonian of the dipolar interaction is given by:

$$H_{dip} = \frac{\mu_0}{4\pi}\frac{\hbar^2\gamma_\mu\gamma_j}{r^3}\vec{S}\cdot\vec{I} - \frac{\left(\vec{S}\cdot\vec{r_j}\right)\left(\vec{I}\cdot\vec{r_j}\right)}{r^2} \tag{3.1}$$

Where

- $\vec{S}$ and $\vec{I}$ are the spin operators of the muon and the nucleus respectively
- γ_j the gyromagnetic ratio of the nucleus j
- r_j is the distance between the muon and the nucleus j, with $r = |\vec{r_j}|$.

This means that the hyperfine interaction and the effect of the nuclear quadrupole moments become negligible (Van Vleck limit). The only interactions that affect the polarization of the muon are the magnetic dipole of the neighboring nuclei and the transverse field itself. Also, it is assumed that the particle does not diffuse meaning the local distribution of magnetic fields in the muon is stable [Vil98]. It shall be seen that the dipolar relaxation is highly dependent on the location of the muon which will allow to compare the experimental results with the *ab-initio* calculations.

Assuming a static distribution of the local magnetic field, it is easy to show that the

polarization will have a Gaussian relaxation:

$$p_x(t) = e^{-\sigma^2 t^2} cos(\omega t + \phi) \tag{3.2}$$

Assuming the above conditions, the relaxation rate, σ can be estimated with the expression:

$$\sigma^2 = \frac{1}{2}\frac{1}{3}\gamma_\mu^2\gamma_j^2\hbar^2\left(\frac{\mu_0}{4\pi}\right)^2\left(\frac{3\cos^2\theta - 1)}{r^6}\right)^2 \tag{3.3}$$

In order to get rid of any axis dependence usually the measurements are done with a powder sample. This means that the angle dependence is no longer prevalent leading to the expression:

$$\sigma^2 = \frac{4}{15}\left(\frac{\mu_0}{4\pi}\right)^2\gamma_\mu^2\hbar^2\sum_{j=1}^{n}\frac{\gamma_j^2 I_j(I_j+1)}{r_j^6} \tag{3.4}$$

Where

- ω is the Larmor frequency, as previously mentioned $\omega = \gamma_\mu B$
- ϕ is the phase.
- θ_J is the polar angle between the nucleus j and the applied magnetic field (see Fig. 3.1).
- n is the number of relevant neighboring nuclei used in the calculation.

3.2 The avoided quadrupole level-crossing technique

The avoided quadrupole level-crossing technique is a very effective tool to proceed to the determination of the muon site, due to its extreme sensitivity to the distance between the muon and the nearest neighboring nuclei. In the presence of an applied longitudinal magnetic field the spin polarization of the muon is kept constant by

the field. Due to this field, the energy levels of the muon particle start to split (Zeeman effect). If the neighboring nuclei carry some quadrupole moment they will exhibit energy splits as well. When the Zeeman energy of the muon matches the quadrupole energy of the neighboring nuclei [1], a resonance effect takes place, coupling the muonic and nuclear spins. This leads to a loss of polarization of the muon. This effect manifests itself through the magnetic dipole-dipole interaction (see Eq. 3.1) which admittedly has a short range ($\propto r^{-3}$), meaning that it usually only reaches the first neighbor of the muon. When this happens, the two particles constitute a system where the original spin states (Fig. 3.2) become mixed. The interaction avoids energy degeneracies, in fact, the strength of the resonance is directly correlated to the energy gaps between the former degenerate states. This effect is evident in figure 3.3 [Cox92].

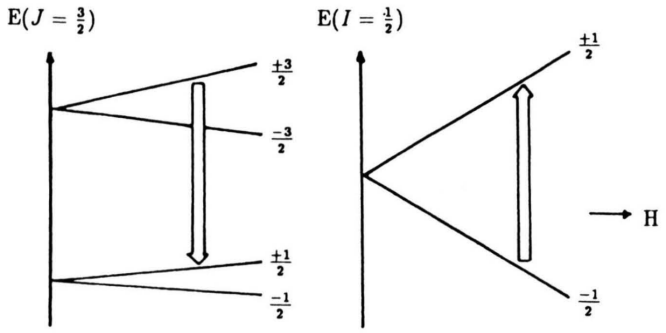

Figure 3.2: The energy states for a $\frac{3}{2}$ spin nuclei (left) and the muon probe (right). From [Cox92]

[1] Note that this is possible because the gyromagnetic ratio of the muon is much larger than that of the proton ($\gamma_\mu = 3.18\gamma_p$)

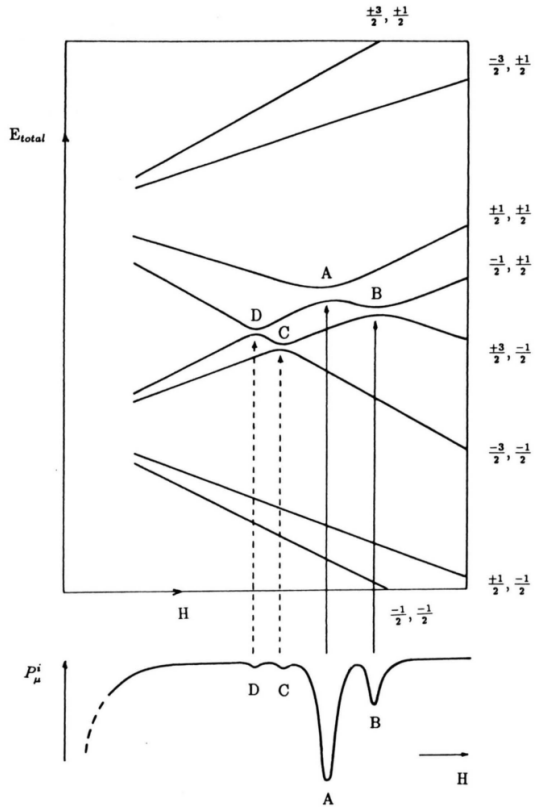

Figure 3.3: The mixed energy states. The lower part of the figure depicts the polarization drops for the different avoided crossings, indicated by the letters. Notice that the bigger the gaps, the bigger the polarization loss. From [Cox92].

The previously mentioned resonance condition can be described by equation 3.5 [Cox92].

$$H_{res} \simeq \frac{|\Omega_q|}{\gamma_\mu - \gamma_n} \simeq \frac{|\Omega_q|}{\gamma_\mu} \tag{3.5}$$

Where H_{res} is the magnetic field and $\Omega_q/2\pi$ the quadrupole splitting in frequency units. Note that in most cases $\gamma_\mu \gg \gamma_n$ which results in the above approximation.

The quadrupole splitting itself is given by [SW95]:

$$\Omega_q = \frac{eQV_{zz}}{4I(2I-1)} \tag{3.6}$$

Where

- Q is the quadrupole moment

- V_{zz} is the electric field gradient

- I is the nuclear spin

Finally, seeing as the quadrupole moment and the nuclear spin are known constants, one can calculate the electric field gradient[2] and consequently estimate the distance between the muon and the nucleus (Eq. 3.7).

$$V_{zz} = \frac{-2ke}{r^3} \tag{3.7}$$

3.2.1 Simulations

During the course of this work we did an intensive use of the *Quantum* wizard script written by James Lord, available in the ISIS *Mantid* software. Here, we inputted parameters that allowed us to define the environment around the muon spin. These included: coordinates of muonium and the neighboring nucleus, their corresponding isotropic and anisotropic hyperfine frequencies, the quadrupole frequency of the nucleus and the longitudinal magnetic field loop. In order for us to get acquainted with the software, several simulations of classical systems were preformed, which are here presented also as an illustration of the avoided quadrupole level-crossing technique.

The use of this technique was first proposed by A. Abragam in 1984 [Abr84]. One of the earliest avoided quadrupole level crossing experiments was performed in ^{63}Cu and ^{65}Cu. Using this technique scientists were able to gather information on the sites occupied by the muon as well as estimate the quadrupole frequency of the copper nuclei [LBK$^+$91]. The following figures 3.4 and 3.5 are the original quadrupole avoided level-crossing pattern as well as the predicted result from our simulation.

[2]This is an approximation, the assumption here is that the electric field gradient is caused by the muon alone, ignoring the contribution of the other particles in the system

^{63}Cu and ^{65}Cu

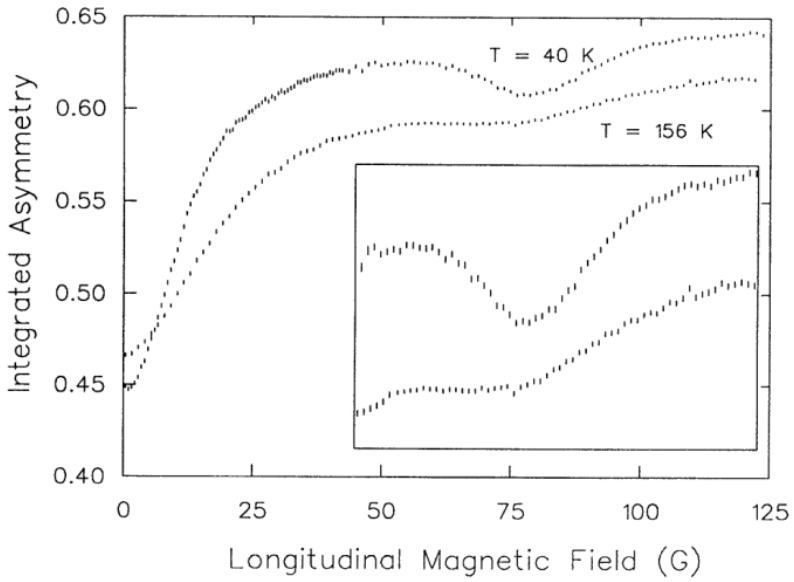

Figure 3.4: The original quadrupole avoided level-crossing pattern for the ^{63}Cu and ^{65}Cu samples from [LBK$^+$91]. The insert depicts an expanded vertical scale.

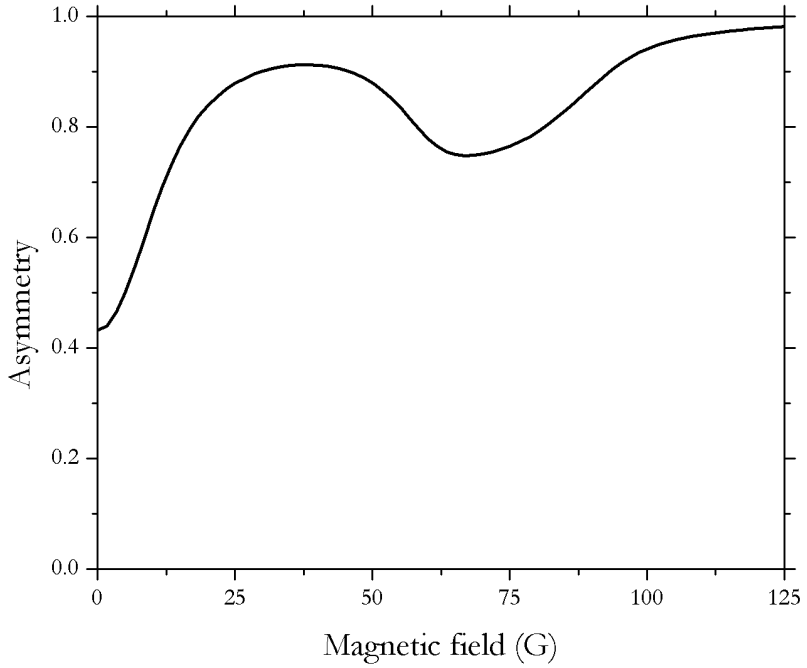

Figure 3.5: The simulated results for the quadrupole avoided level-crossing pattern for the ^{63}Cu and ^{65}Cu samples from [LBK$^+$91].

3.2.2 Additional simulations in the presence of an hyperfine interaction

Level crossing of the muonium system: the effect of the hyperfine interaction

The presence of a hyperfine interaction leads to additional resonance phenomena. The dip in polarization now lies on magnetic fields with much greater orders of magnitude (10^4 G).

Although the following simulations no longer constitute illustrations of the quadrupole avoided level-crossing technique they were essential in getting us familiarized with the *Mantid* software [ABB+14]. These represent an essential step in verifying the veracity of the output of the *Mantid* program.

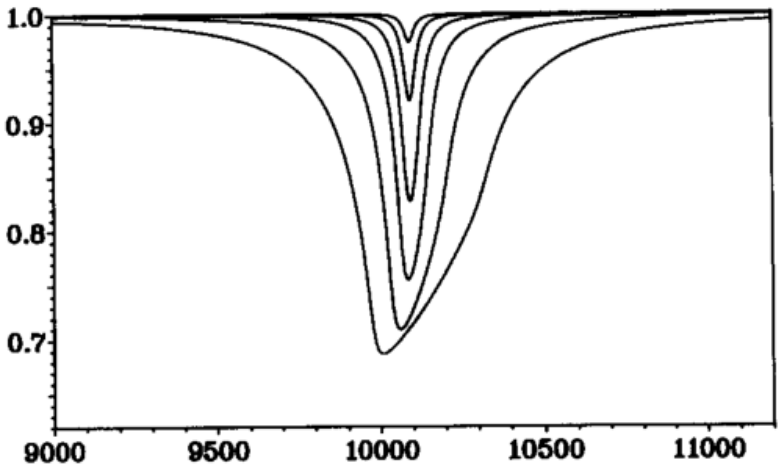

Figure 3.6: Avoided level-crossing powder pattern for the muon and electron system with an hyperfine constant of A_{iso} = 275 MHz. The anisotropic hyperfine component, $D_{||}$ is 6, 3, 0.5, 0.4, 0.2 MHz from the broader to the narrower curves. From [RPM+95].

In figure 3.6 we present an avoided level-crossing pattern of a powder system for several values of $D_{||}$, from ref. [RPM+95]. Our own simulation of the same avoided level-crossing pattern is shown in figure 3.7 for the $D_{||}$ = 6 MHz curve (broader curve in Fig. 3.6).

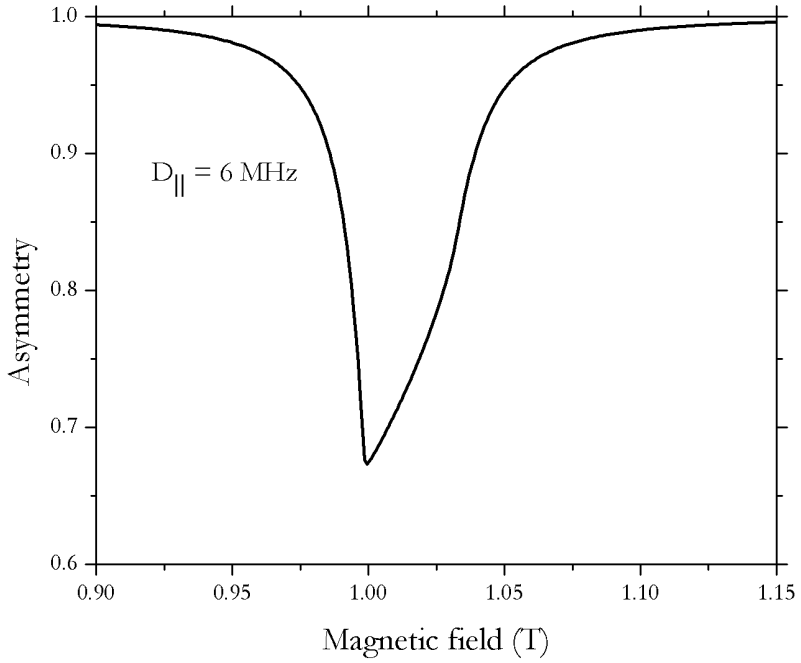

Figure 3.7: Our simulations of an avoided level-crossing powder pattern for the muon and electron system with an hyperfine constant of $A_{iso} = 275$ MHz. The anisotropic hyperfine component, $D_{||}$ is 6 MHz. From [RPM$^+$95]

Level crossing of muonium and a nucleus system in the presence of a hyperfine interaction

The interaction between a muonium system and a nucleus will yield several spin flip and spin flop phenomena resulting of the hyperfine interaction. These resonances are governed by selection rules. In particualr, the selection rule $\Delta M = 0$ determines muon-nuclear spin flip flop transitions due to an isotropic hyperfine interaction. Furthermore, the anisotropic component of the interaction drives two additional types of resonance: a single particle muon or nuclear spin flip $\Delta M = 1$ and a muon-nuclear spin flip-flip $\Delta M = 2$.

Below is depicted the original avoided level-crossing powder pattern of a system composed of a muon and a proton and its corresponding simulation (Figures 3.8 and 3.9, respectively) [KR95].

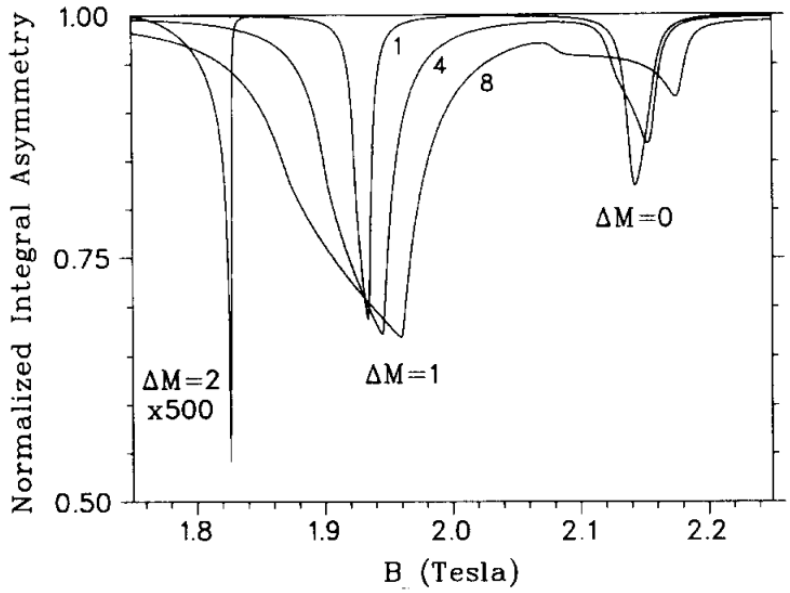

Figure 3.8: The original avoided level-crossing pattern for the muon and proton system. The isotropic hyperfine constants are $A_\mu = 526$ MHz and $A_p = 125$ MHz. The anisotropy dipolar interaction of the proton is fixed at $D_p = 2$. Different muon dipolar hyperfine constants ($D_\mu = 1, 4, 8$) are depicted. The $\Delta M = 2$ line for $D_\mu = 8$ is expanded 500 times. From [KR95]

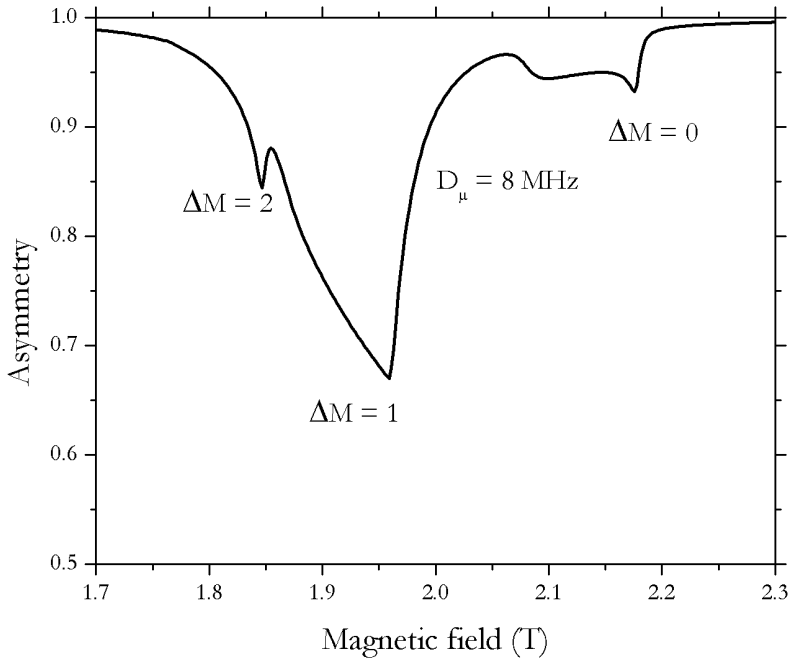

Figure 3.9: Our simulation of the avoided level-crossing pattern for the muon and proton system shown in figure 3.8, using $D_\mu = 8$ MHz.

4

Results and discussion

4.1 Experimental context

As mentioned in section 1.3, the aim of this work was to characterize the positively charged configuration in BeO by using its analogue the muon particle. As explained in chapter 2, the positive muon behaves chemically as the proton and can thus be used as a light pseudo-isotope. Muon spin spectroscopy experiments were performed at the HiFi instrument in the ISIS facility in the United Kingdom in September 2017.

This experiment was focused in the clarification of the positively charged configuration Mu^+ (although some measurements regarding neutral muonium, Mu^0 were included). In particular, we attempted to characterize its thermal stability by following the temperature dependence of the μSR signal (in particular the asymmetry) in transverse field geometry (B = 95 G). Temperatures were swept in a range between 0 and 700 K. We also attempted to observe the avoided level-crossing of the diamagnetic Mu^+ configuration with nearby ^{9}Be nuclear quadrupole moments in order to characterize the site occupied by Mu^+. This was done by performing a small step sweep of the longitudinal magnetic field (ranging from 0 to 250 G) in order to find the value at which the resonance effect took place. Finally, we also tried to recover the missing fraction of the signal with the intention of characterizing the interaction(s) responsible for the disappearance of the muon signal. To characterize this component we extended the longitudinal field measurements up to 1.1 T in order to recover the missing fraction and estimate the strength of the depolarizing

interaction(s).

It is important to stress that the repolarization measurements, as we shall explain below, allow a deeper understanding of the neutral muonium, Mu^0 configurations. As we mentioned in section 1.3, these configurations have already been investigated before (2014) by the Coimbra μSR group. The basic characterization of the neutral configuration revealed an isotropic center with hyperfine interaction A = 4451.2(2) MHz. This value is close to that of muonium in vacuum and consistent with the H^0_{int} ground configuration addressed in section 1.3 (Fig. 1.7) [MVV$^+$17][Vie18]. Although the results of this former experiment were centered around the neutral configuration, they contain as well some relevant information on the positively charged configuration which is the main topic of this dissertation. Some of the relevant unpublished results of the PSI experiment were therefore reanalyzed and included here whenever necessary.

4.2 General analysis overview

For the μSR experiments at the HiFi instrument at ISIS, both a single crystal (Fig. 4.1) and a powder sample (Fig. 4.2) of BeO were used. The single crystal was the same used in the PSI experiments (high purity single crystal grown by V. A. Maslov using a modified solution-melt method under reverse temperature drop conditions [MVV$^+$17]). The powder sample was a polycrystalline sample acquired commercially (Alfa Aesar, 99.95%).

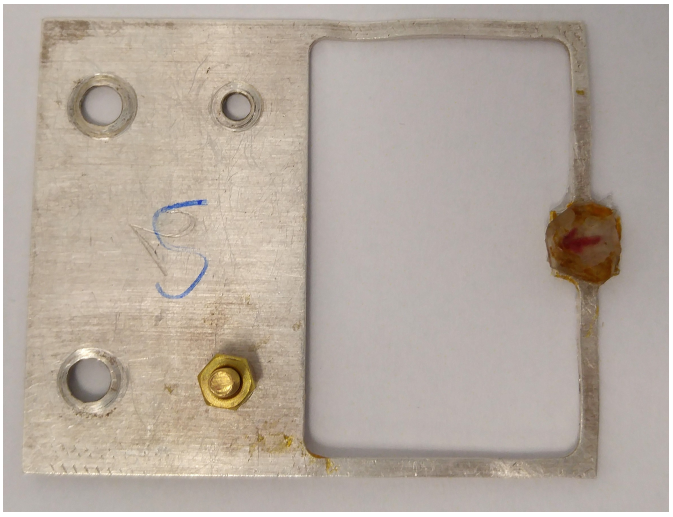

Figure 4.1: BeO sample (mounted on a silver sample holder) used in both the PSI and ISIS experiments. The red arrow indicates the crystallographic [1, -1, 0] orientation. The c axis is perpendicular to the surface.

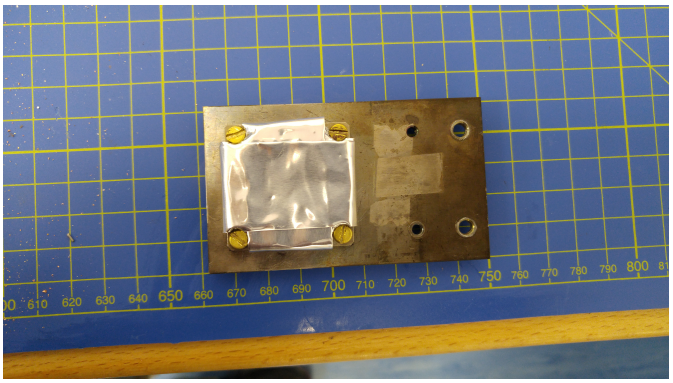

Figure 4.2: BeO powder sample in a titanium structure surrounded by an aluminum foil wrap to prevent spillage.

The initial analysis was done using a software called WiMDA (Windows Muon Data Analysis) [Pra00]. As it was previously mentioned, the detectors at ISIS are able to measure events that span across several muon lifetimes. This is particularly relevant for the diamagnetic fraction[1] of the μSR signal. The small depolarization associated with the isolated muon can be traced to the magnetic dipole interaction with the neighboring nuclei. This relaxation is rather small and can therefore be better defined throughout longer time frames.

[1] In μSR, diamagnetic and paramagnetic are, respectively, the typical designations of the muon and muonium fractions of the signal.

After analyzing the data with just this one component we quickly came to the conclusion that some other fast relaxation mechanism was also taking place. This is apparent as an additional relaxation component of the same diamagnetic frequency. Henceforth we added a second, fast relaxing component. Nonetheless the fast nature of the component is an indication of an interaction with electrons and of a paramagnetic character. Fast relaxing signals like this are better defined for earlier time frames.

The presence of muonium can not be directly picked up by the HiFi instrument (see the end of section 2.2) and constitutes a missing fraction in magnetic transverse field measurements. The absence of a signal is evident when comparing transverse field runs of the sample with those of silver. In longitudinal field measurements this missing fraction can be recovered which allows us to have an idea of the strength of the interaction (see section 2.4). The analysis of the μSR signal in ISIS was therefore based on two components: a slow relaxing component associated with the diamagnetic state and a fast relaxing component associated with a diamagnetic-like state. The fit function used is given by equation 4.1

$$A(t) = A_s e^{(-\sigma t)^2} \cos(2\pi f_s t + \phi_s) + A_f e^{-\lambda t} \cos(2\pi f_f t + \phi_f) \tag{4.1}$$

Where

- A_s and A_f are the asymmetries of the slow and fast component respectively;
- σ and λ are the relaxations of the slow and fast components, respectively;
- f_s and f_f are the respective precession frequencies;
- ϕ_s and ϕ_f are the respective phases;

Despite both components precessing at the diamagnetic Larmor frequency (Eq. 2.2), in a first analysis step we let both f_s and f_f as free parameters in order to check for possible frequency shifts. However no significant difference was found which prompted us to fix the frequencies to the same value in the final analysis. The gaussian shape of the relaxation of the slow component is that expected from broad-

ening due to the dipolar interaction with nearby nuclear magnetic moments. The Lorentzian shape of the relaxation of the fast component is also that expected from the Poisson-like nature of the interaction with fluctuating electrons.

In figure 4.3 we can clearly see the two components at play. The slow is the dominant one and constitutes most of the signal. The fast component still has a significant contribution, despite dropping off rather quickly for short times.

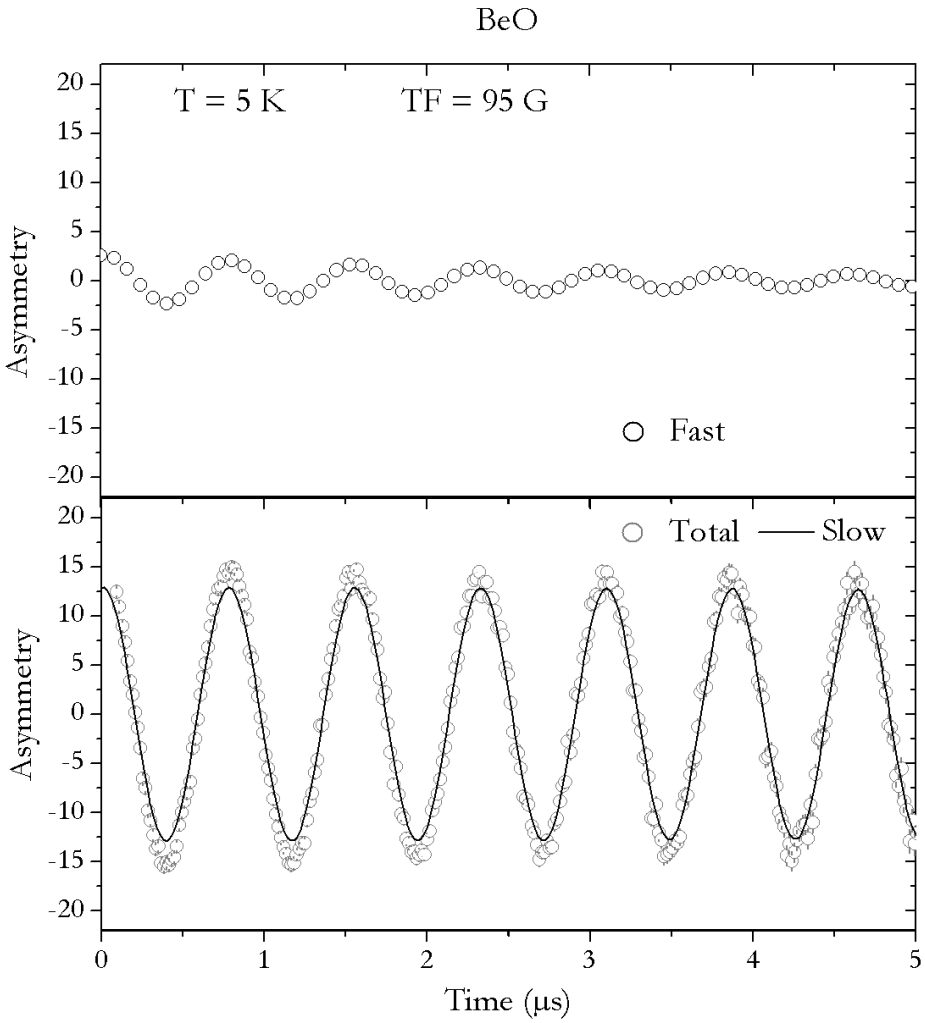

Figure 4.3: The time spectrum of the μSR signal of BeO with a transverse magnetic field of 95 G and a temperature of 5 K limited to 5 μs only. The total time spectra is plotted in the bottom frame together with a line representing the slow component as fitted (Eq. 4.1). The upper frame represents the remaining fast component (resulting of the subtraction of the line to the total time spectra in the bottom frame).

The muon does not exhibit any significant relaxation or missing fraction in silver

and therefore we can extract the maximum instrumental asymmetry from calibration measurements in this material, as mentioned in the end of chapter 2. Comparing the total BeO signal with that of the silver sample brings out the existence of a missing fraction of the muon spin polarization (Fig. 4.4), connected with the formation of the muonium state known from the previous experiments at PSI.

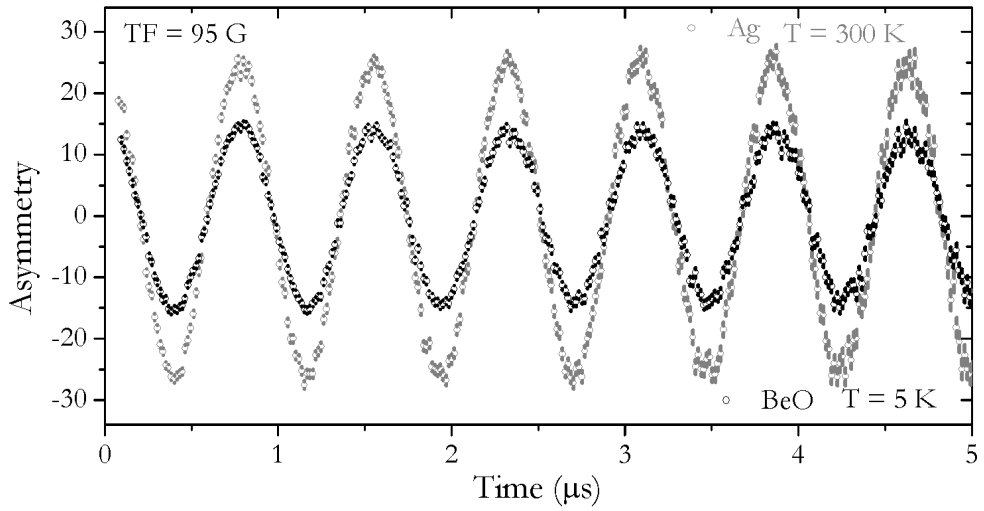

Figure 4.4: The time spectrum of the μSR signal of BeO with a transverse magnetic field of 95 G at a temperature of 5 K (black circles) overlapped with the time spectrum of the μSR signal of a silver sample with a transverse magnetic field of 95 G at a temperature of 300 K (gray circles). The difference in asymmetries is a result of the muonium signal, undetectable at ISIS.

As mentioned above, some unpublished data taken at PSI contain important information about the positively charged configuration. We have included these here, upon our reanalysis. These data were acquired at the GPS instrument in transverse field geometry at B = 15 G. Besides the slow and fast components precessing at the known Larmor frequency, as seen at ISIS we now observe a further precessing component at $f_\mu \simeq 23$ MHz corresponding to lines ω_{12} and ω_{23} of muonium (see Fig. 2.4). These data were analyzed with a fit function with three components as follows:

$$A(t) = A_s e^{(-\sigma t)^2} \cos(2\pi f_s t + \phi_s) + A_f e^{-\lambda t} \cos(2\pi f_f t + \phi_f) + A_\mu e^{-\lambda_\mu t} \cos(2\pi f_\mu t + \phi_\mu) \tag{4.2}$$

Where

- A_μ is the asymmetry of the muonium component;
- λ_μ is the relaxation of the muonium component;
- f_μ is the respective precession frequency;
- ϕ_μ is the respective phase;

A detail of the time spectra of this signal, evidencing the muonium oscillation, as well as the corresponding three component fit is depicted in figure 4.5.

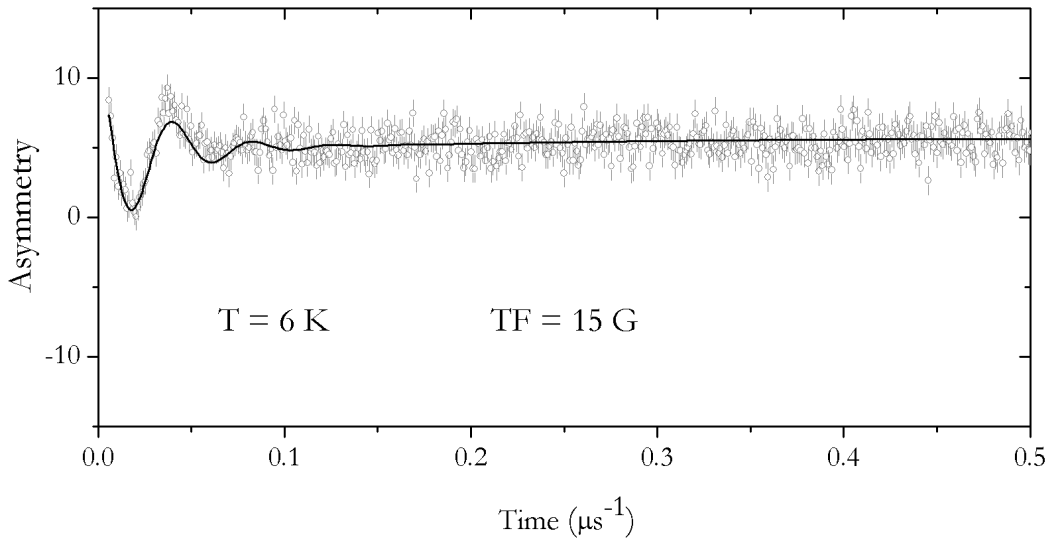

Figure 4.5: The time spectrum of the μSR signal of BeO taken at the GPS instrument at PSI, with a transverse magnetic field of 15 G at a temperature of 6 K (gray circles). The relaxed Mu oscillation at $f_\mu = 23$ MHz is clearly visible, superimposed at the diamagnetic frequency (not visible in the selected time window of this plot)

4.3 Temperature stability measurements

4.3.1 Results

We begin by presenting the experimental results related to the characterization of the muon under different temperatures. From a preliminary analysis we concluded that the precession frequencies of the slow and fast component were the same and practically constant at an effective field of 95.627(5) G (Fig. 4.6). The phase of the slow component was also deemed constant at -6.27(6) deg. In order to better define the fast component, we started by fitting the slow relaxing component from 3-25 μs. This way, we isolated the slow component and properly defined its asymmetry and relaxation (the precession frequency and phase were fixed to the previously mentioned values). The slow component parameters were then fixed and a second fast Lorentzian relaxing component was added and fitted from 0-25 μs (having fixed the precession frequency to that of the slow component). This left the asymmetry, relaxation and phase of the fast component as free parameters. The relaxation of the fast component was found to be mostly constant with temperature and was henceforth fixed. The phase and asymmetry of the fast component were subsequently obtained.

The final asymmetries were then converted to formation fractions (Fig. 4.7 and Fig.4.8) by normalizing them to the maximum instrumental asymmetry, obtained from silver calibrations. The temperature dependence of the relaxations of the slow and fast components are presented in Fig. 4.9 and Fig. 4.10, as a result of the aforementioned analysis. The corresponding temperature dependence of the phases is depicted in figures 4.11 and 4.12, respectively.

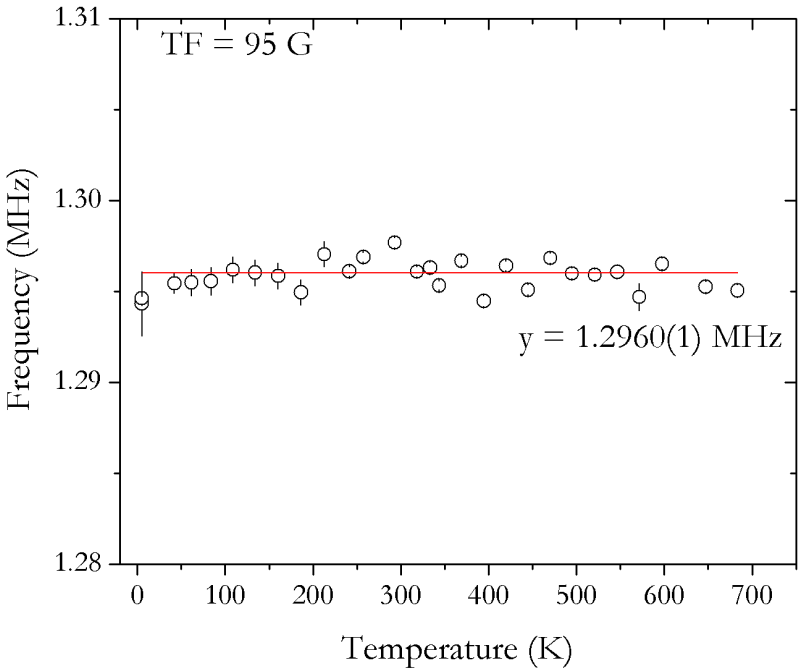

Figure 4.6: Temperature dependence of the common precession frequency of the slow and fast components. The solid line represents the assumed constant value for the frequency which is equivalent to an effective field of 95.627(5) G.

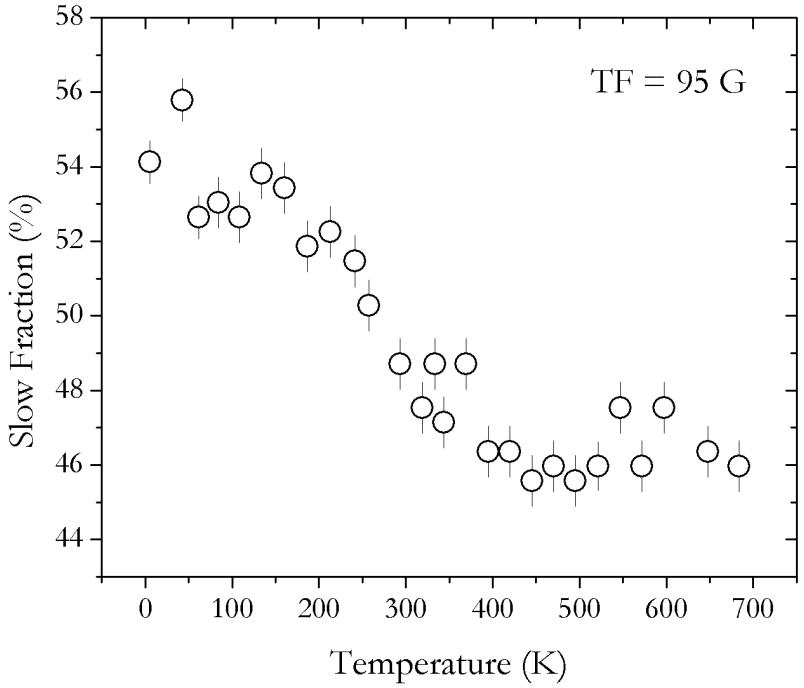

Figure 4.7: Temperature dependence of the slow fraction of the μSR signal.

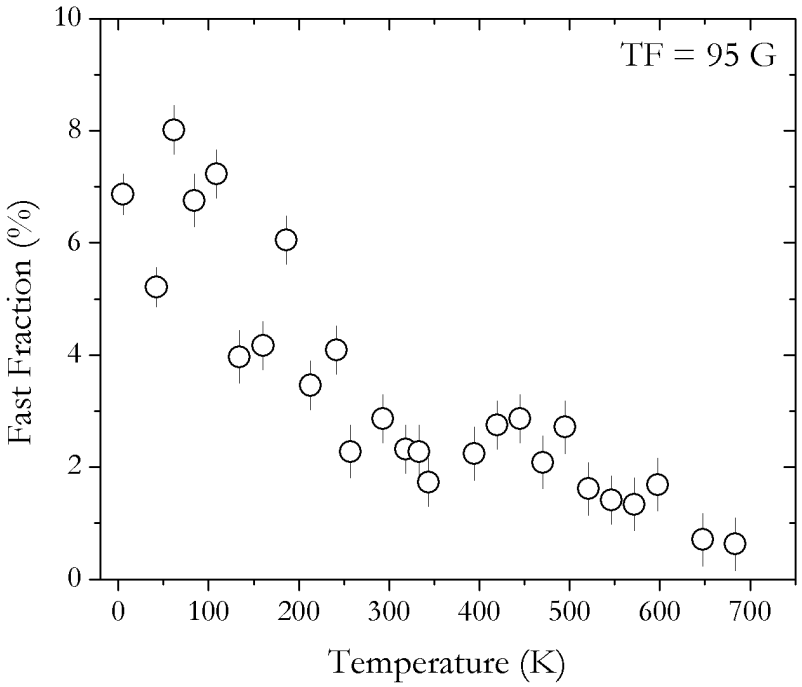

Figure 4.8: Temperature dependence of the fast fraction of the μSR signal.

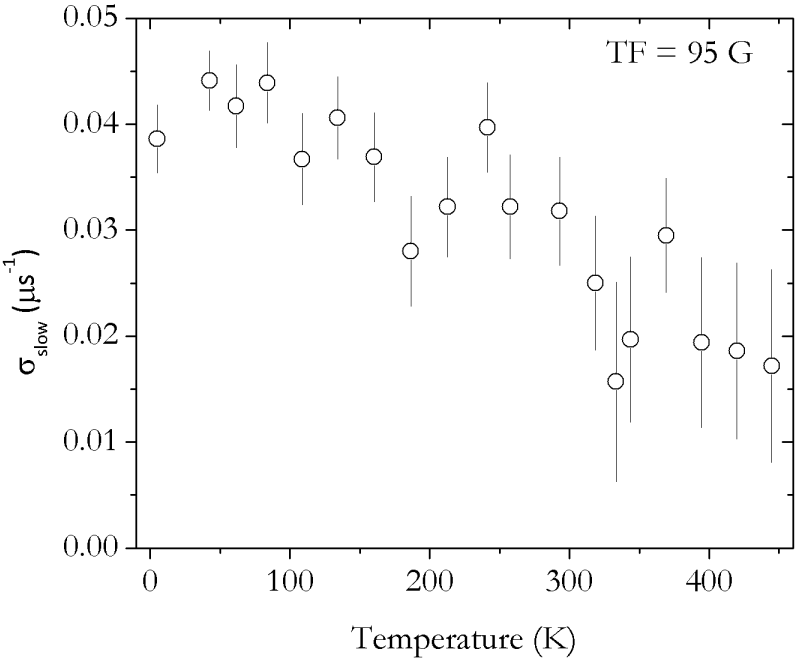

Figure 4.9: Temperature dependence of the relaxation of the slow component for low temperatures.

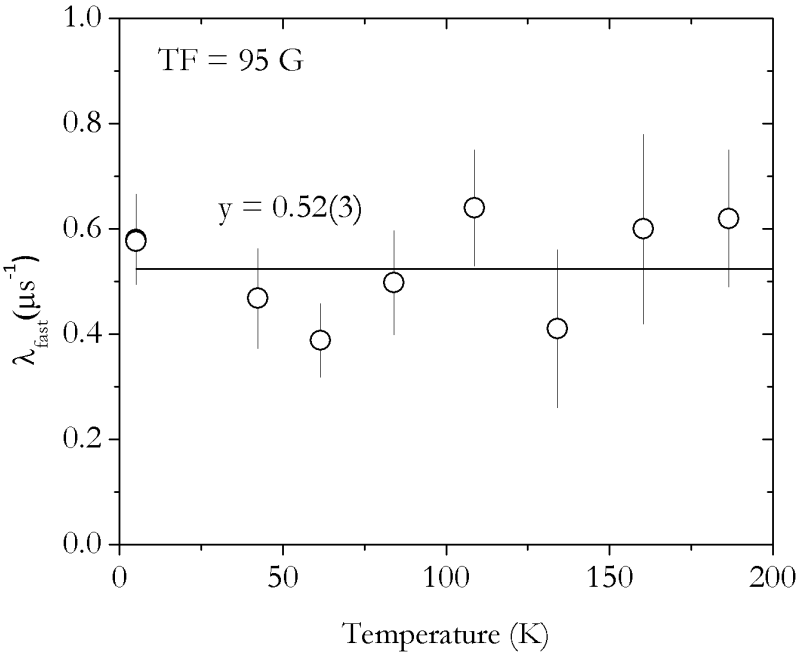

Figure 4.10: Temperature dependence of the relaxation of the fast component. The fast fraction is close to zero for higher temperatures and thus in this region, fitting parameters lose significance. Up to 200 K this relaxation is practically temperature independent at 0.52(3) μs^{-1}.

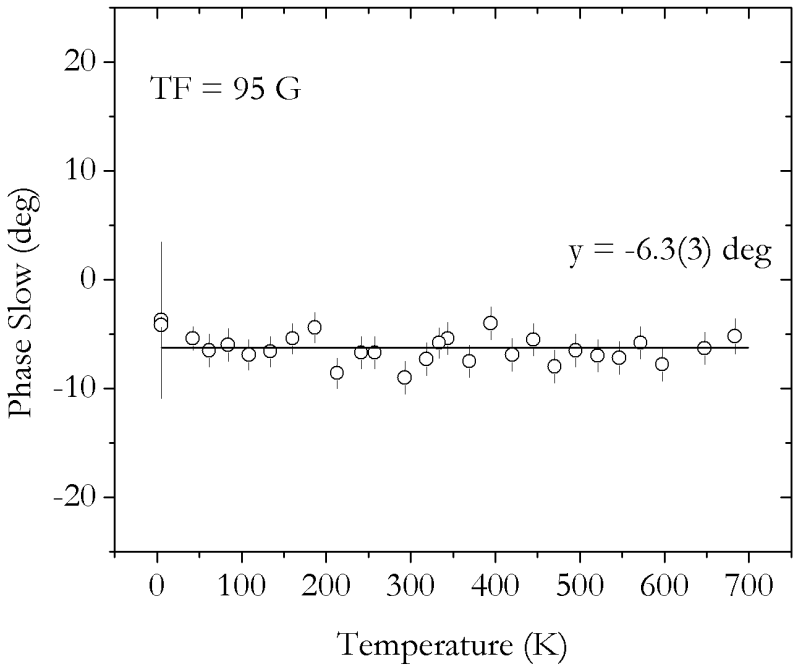

Figure 4.11: Temperature dependence of the phase of the slow component. The solid line represents the assumed constant value for the phase -6.3(3) degrees.

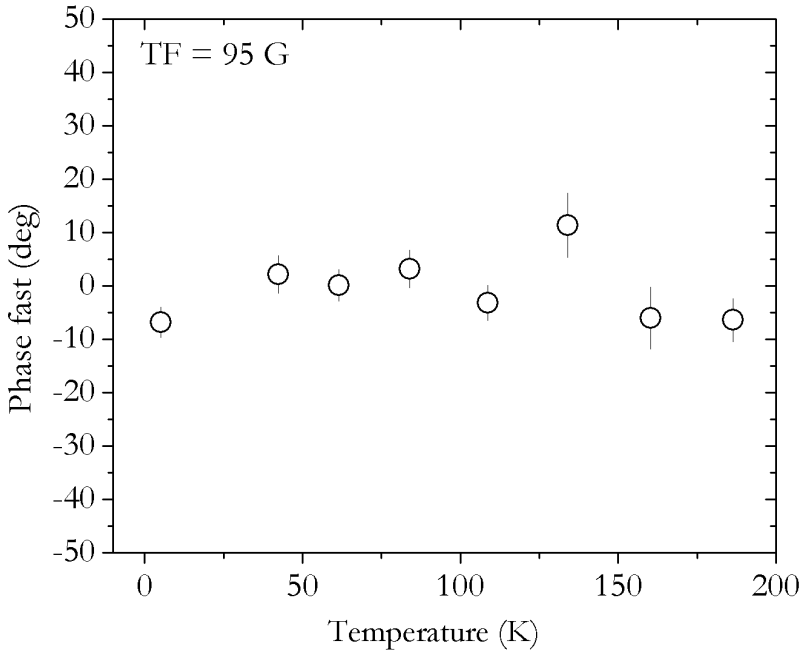

Figure 4.12: Temperature dependence of the phase of the fast component. The fast fraction is close to zero for higher temperatures and thus in this region, fitting parameters lose significance.

4.3.2 Data analysis

Fraction analysis

For temperatures up to 150 K the slow fraction is constant somewhat around 54% (Fig. 4.7). However, as temperature increases there is a visible drop until around 450 K where it becomes constant again at 46%. The fast fraction also exhibits a similar behavior, decreasing from 7 to 2% between 100−300 K. This means that the fraction of the unobserved muon spin polarization (missing fraction) increases from 39% to 52% around this temperature range.

In a first approach, the decay in the slow fraction with increasing temperature may be fitted to a thermally activated process with a Boltzmann-like model described by a single activation energy (Eq. 4.3):

$$f_d = \frac{f_0}{1 + N^{-E_a/k_B T}} + B \tag{4.3}$$

Where,

- f_d is the diamagnetic fraction
- f_0 is the conversion fraction
- N is an effective density of states for the process
- E_a the activation energy
- B is a background component corresponding to a diamagnetic fraction no involved in this process (see discussion in section 4.6.2)

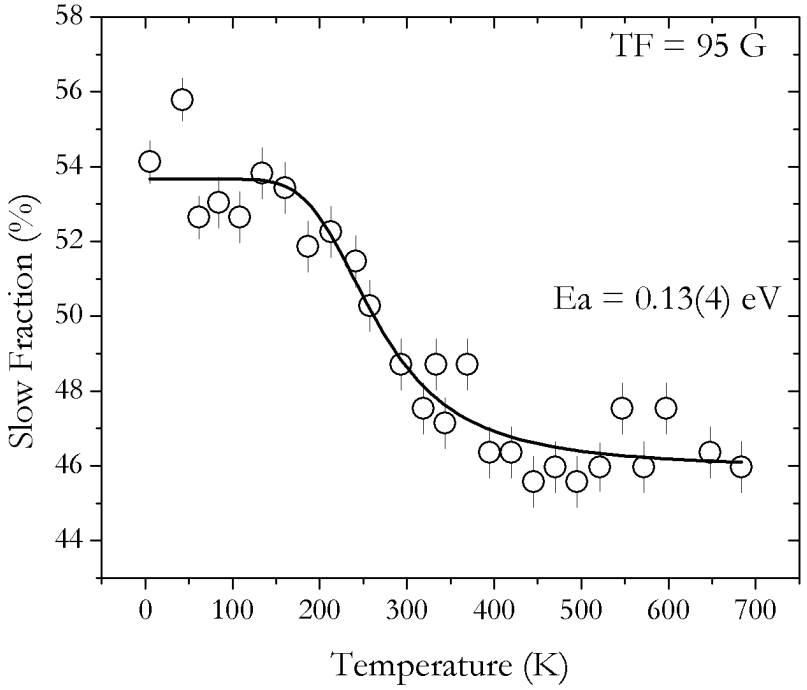

Figure 4.13: Temperature dependence of the slowly relaxing diamagnetic component. The line is a fit to equation 4.3.

The resulting activation energy is around 0.13(4) eV with N = 253,4 (fixed). This means that a low energy barrier must be overcome in order to convert part of the slow fraction into the missing fraction.

Relaxation analysis

In order to further characterize the nature of the slow component we compared the experimental values of the slow relaxation (Fig. 4.9) with the expected value for the relaxation due to dipolar broadening arising from nearby nuclear moments (the Van Vleck limit introduced in section 3.1)[GMF+99]. It is important to mention that the *ab-initio* study, referred in section 1.3, also estimated the relative distances between the different muon sites and its neighboring atoms[2]. With these values it is possible to compute the theoretical relaxation values in the Van Vleck limit for different Mu^+ sites. The final results of the theoretical Van Vleck calculations are hereby presented in table 4.1.

State	Formation energy (eV)	σ (MHz)
$H^+-OH_{\|\|}$	-	1.53×10^{-2}
$H^+-ABO_{\perp}$	0.46	1.67×10^{-2}
$H^+-OH_{\perp}$	0.54	1.86×10^{-2}
$H^+-ABO_{\|\|}$	0.65	1.99×10^{-2}

Table 4.1: The relaxations rates for the different diamagnetic states.

These results were calculated with the van Vleck model for a polycrystalline sample and are more easily comparable with the value of the relaxation obtained for the slow component in the repolarization measurements (presented further ahead) with powder samples. At the lowest temperature (T = 5 K) $\sigma_{slow} = 0.025(2)\mu$ s^{-1}. The values obtained for the relaxation of the slow component in the transverse field measurements are slightly higher but of the same order of magnitude. The order of magnitude of these results clearly indicates that indeed the observed relaxation arises from nuclear dipolar broadening. It is difficult to be more precise based on these data but the observed value of the relaxations both in the single-crystalline transverse field data at 100 G and in the polycrystalline longitudinal field data at the very low fields (up to 10 G) suggest that the value of the relaxation is much higher than that predicted for Mu^+ in the ground state ($H^+-OH_{||}$).

[2]These tables are available in Appendix 1

Furthermore, it was possible to do an angle dependent measurement in the single-crystalline sample in order to check the dependence of the relaxation with the orientation of the magnetic field with respect to the crystallographic axis [CGR+77]. This was preformed in 2014 at the GPS instrument at PSI, for a transverse field B = 5200 G. The magnetic field was initially applied parallel to the c-axis (perpendicular to the surface of the sample) and was then gradually turned in the [1, -1, 0] direction, in the plane formed by this direction and the c-axis, while forming an angle θ with [0, 0, 1]. The results for the relaxation of the slow component are shown in figure 4.14.

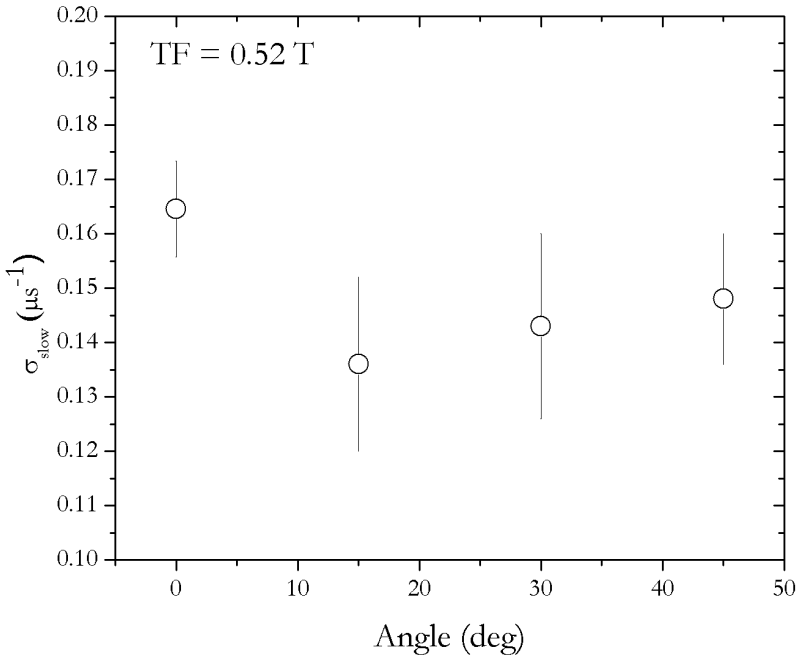

Figure 4.14: The slow relaxation with respect to the orientation of the crystal.

As can be seen from figure 4.14 the relaxation of the slow component is rather high, which we attribute to an instrumental effect as slow relaxations are rather hard to define at PSI. This is due to a non-negligible contribution from the background and the sample-holder which are likely to affect the small value of the relaxation[3]. Most importantly no significant angular dependence is observed. The apparent lack of an angle dependence has also been reported in I-III-VI_2 chalcopyrite semiconductors [GMF+99]. Here, the consensus was that this behavior was a manifestation of

[3]This is basically a consequence of the nature of the beam which is discussed in section 2.3

an anti-bonding configuration. As described in the *ab-initio* calculations this is a possible Mu^+ configuration for BeO. Taking this into account we suggest that a similar configuration is being manifested in our sample.

4.4 Repolarization measurements

4.4.1 Results

In order to characterize the missing fraction we applied the repolarization technique in longitudinal geometry. The increase in longitudinal magnetic field restores the initial polarization of the muons as explained in section 2.4.

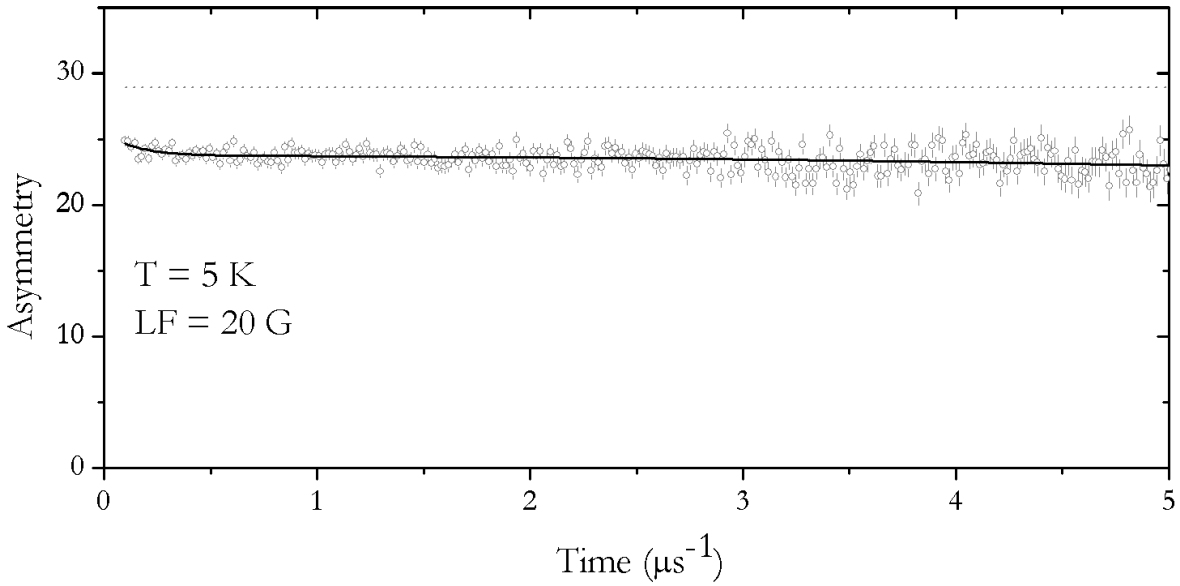

Figure 4.15: The time spectrum of the μSR signal of BeO taken at the HiFi instrument at ISIS, with a longitudinal magnetic field of 20 G at a temperature of 5 K (gray circles). The fast relaxing component at $\lambda = 0.65\ \mu s^{-1}$ is clearly visible. The maximum instrumental asymmetry (obtained from the titanium sample holder measurements at T = 300 K and LF = 10 G) is the dotted gray line at 28.5(6).

The repolarization data was analyzed with the WiMDA software as well. The same strategy as the transverse field measurements was used: isolating the slow fraction between 3-25 μs and then fixing its parameters for a 0-25 μs fit which now included the fast component. These measurements were performed with a powder sample

to eliminate any possible axis dependence. We also performed runs for several temperatures to investigate the shape of the repolarization curve with temperature.

The data were now analyzed with a sum of two relaxing components as such:

$$A(t) = A_s e^{(-\sigma t)^2} + A_f e^{-\lambda t} \tag{4.4}$$

Identically to the transverse field measurements, the obtained asymmetries A_s and A_f were normalized to the maximum instrumental asymmetry (obtained from a calibration run with the empty titanium holder). The corresponding fractions, f_s and f_f are represented in figure 4.16 for the highest and lowest temperatures and in figure 4.17 for the remaining temperatures.

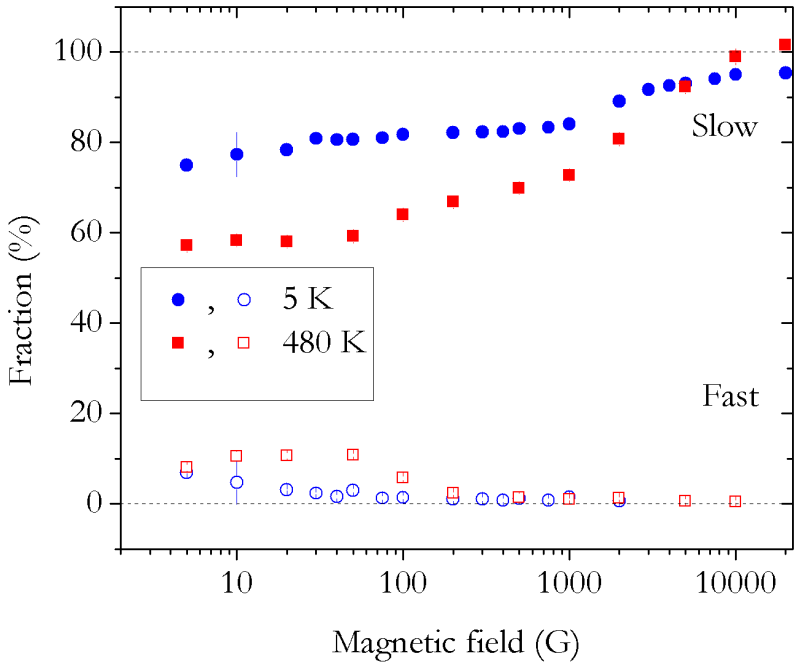

Figure 4.16: Upper and lower temperature limit for the repolarization plots.

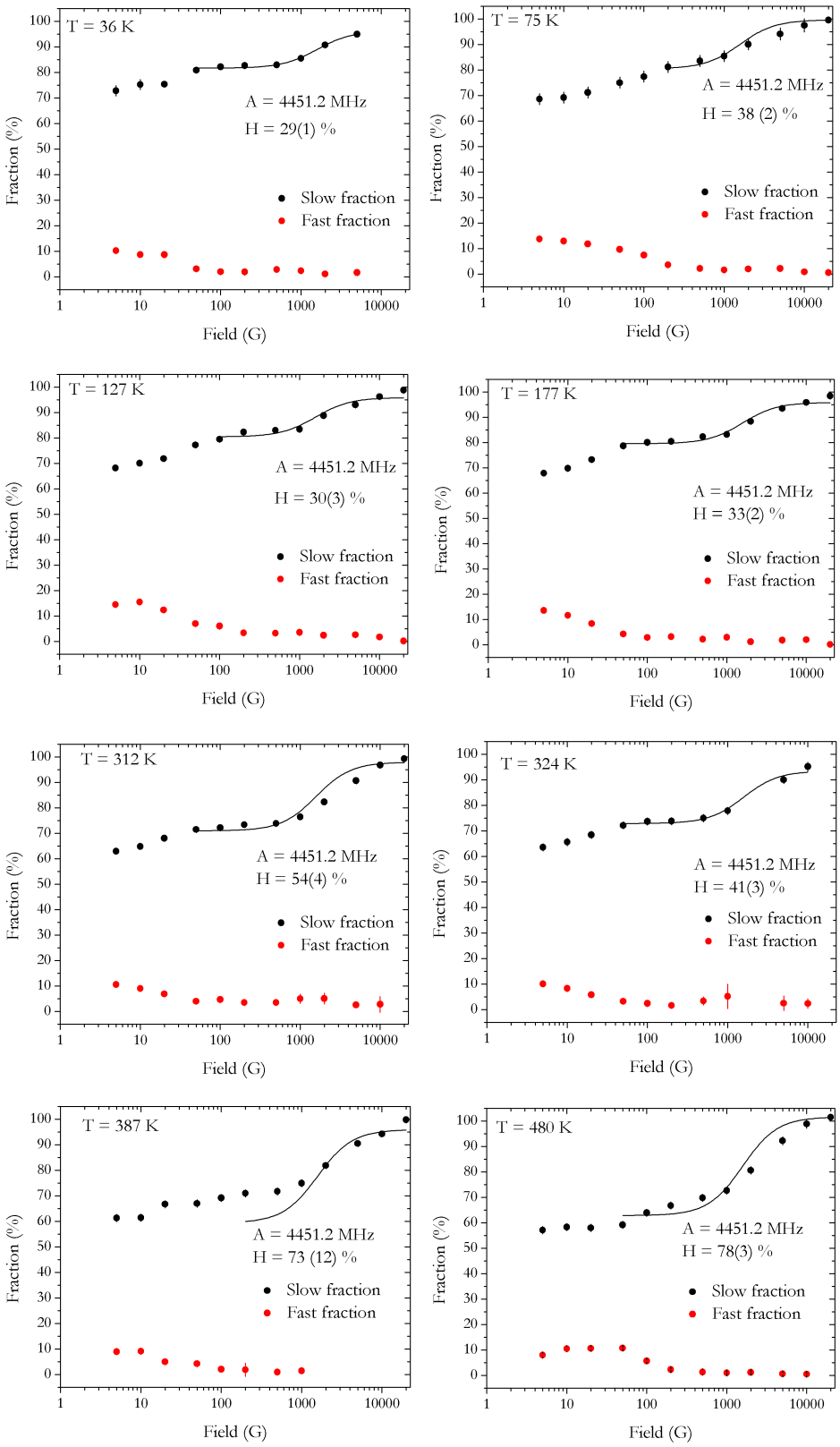

Figure 4.17: Fractions of the slow and fast components in the longitudinal field repolarization experiments. The lines are fits of the isotropic muonium function (Eq. 2.15) to the high field step for several temperatures as described in the text

The slow fraction increases with temperature as expected from the transverse field measurements. The fraction also increases with respect to the field, as expected when the Zeeman effect becomes dominant over the hyperfine interaction. We are also able to observe a two step process (around 50 G) in the repolarization, mainly in the lower temperature plots.

4.4.2 Data analysis

As seen in the transverse field data, we had about 36% of a missing fraction at low temperatures, which is due to muonium formation (known from high field measurements at PSI with $A_{iso} = 4451.2$ MHz).

Despite not being the main object of our study, important information can be drawn from these longitudinal field data regarding muonium formation and dynamics. An isotropic static muonium function can be fitted to the longitudinal field repolarization data with a fixed muonium hyperfine interaction of $A_{iso} = 4451.2$ MHz. As we can see, the isotropic muonium repolarization fit worsens as temperatures increase. We interpret this as a sign that for higher temperatures additional muonium dynamic is taking place. Analyzing this behavior is beyond the scope of this project and further studies will be necessary to fully characterize this dynamic. This matter will be brought up again in section 5.1.

The effect of temperature on the repolarization curve can be better evidenced from a more detailed analysis to the curves at the lowest and highest temperature.

Low temperatures

In the lowest temperature, 5 K, the low field step fits to a very small hyperfine interaction (9 MHz). However, this interaction is probably underestimated since the fit clearly overestimates the corresponding fraction (42%) (Fig. 4.18).

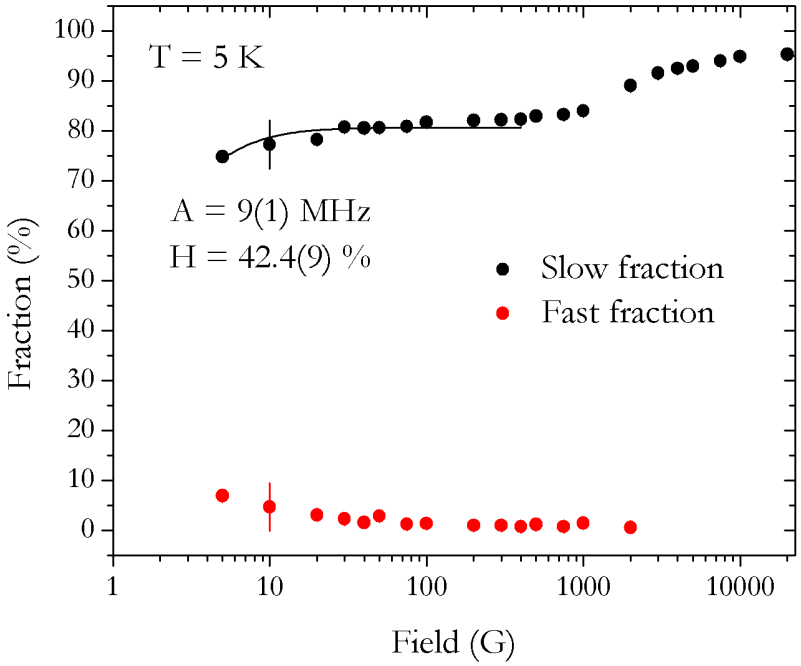

Figure 4.18: Fitting of the isotropic muonium repolarization function to the low field step with temperature at 5 K.

The high field step is consistent with the known hyperfine interaction, 4451.2 MHz. The fitted fraction is 27(1)%, slightly lower than the observed 36% at TF 95 G (Fig. 4.19).

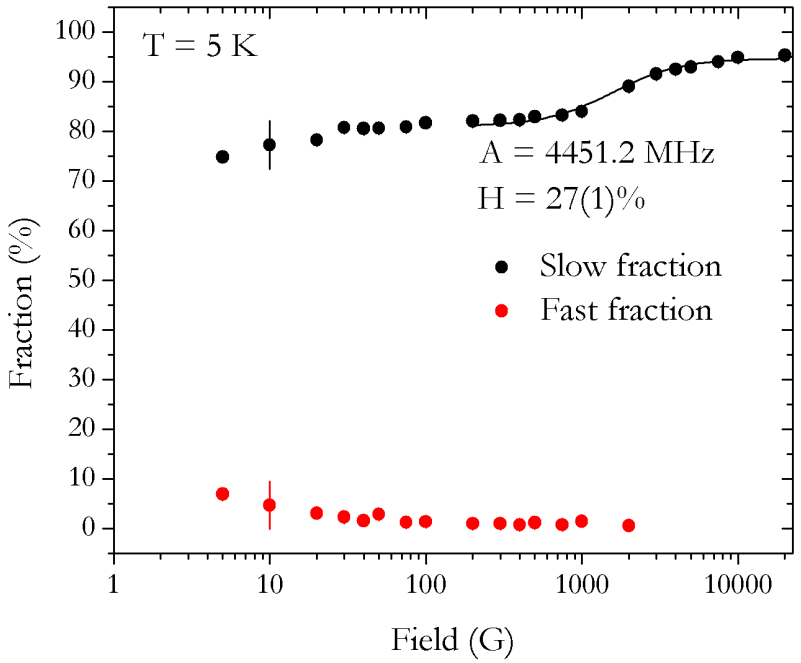

Figure 4.19: Fitting of the isotropic muonium function to the high field 5 K repolarization with a fixed hyperfine parameter (4451.2 MHz).

The relaxation σ of the slow component (Fig. 4.20) is only clearly defined for the lowest fields and is quickly decoupled as the field increases. This is a clear sign of a static interaction such as that arising from the distribution of fields from nearby nuclear dipolar magnetic moments. The value of the relaxation for T = 5 K, B = 5 G is $\sigma = 0.025(2)\mathrm{s}^{-1}$. In contrast, the relaxation λ of the fast component is not much affected by the field at least up to $\sim$ 100 G (4.21).

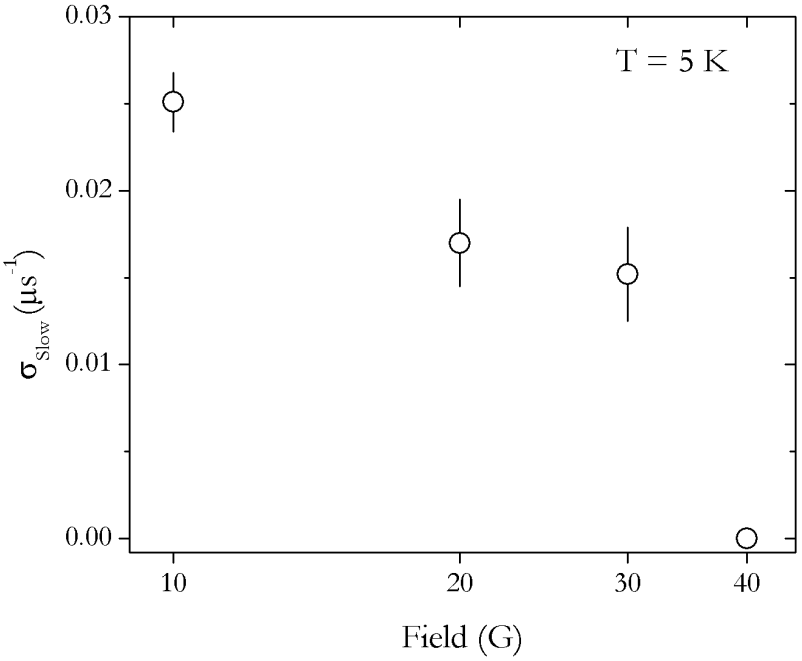

Figure 4.20: The semilogarithmic plot of the relaxation of the slow component with respect to the applied longitudinal field, at T = 5 K. For fields over 30 G the relaxation drops to zero.

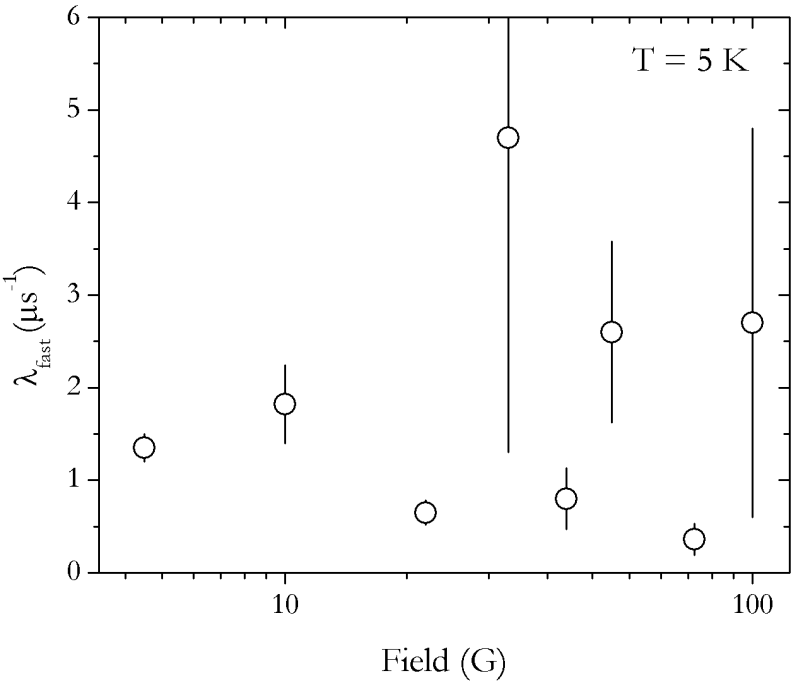

Figure 4.21: The semilogarithmic plot of the relaxation of the fast component with respect to the applied longitudinal field, at T = 5 K. The fit loses significance for values over 100 G because the fast fraction starts to disappear.

High temperatures

Regarding the highest temperature, 480 K, the high field step hyperfine parameter fits to 7 GHz with a 68% fraction (Fig. 4.23). This is inconsistent with the previous hyperfine interaction measurements (4451.2 MHz) performed at PSI and is also an indication of additional muonium dynamic. The low field step hyperfine interaction fits to around 200 MHz (Fig. 4.22).

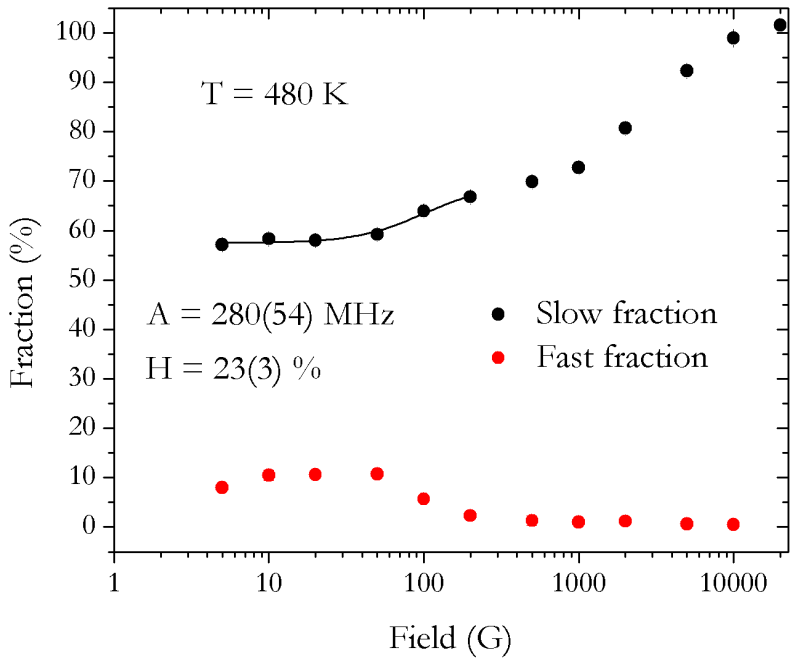

Figure 4.22: Fitting of the isotropic muonium function to the low field 480 K repolarization.

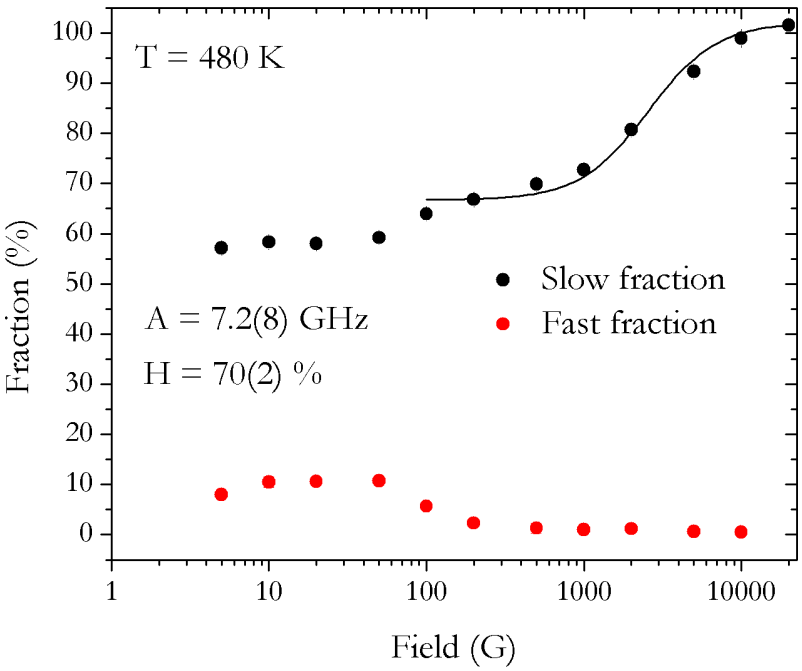

Figure 4.23: Fitting of the isotropic muonium function to the high field 480 K repolarization.

4.5 Characterizing the site of the diamagnetic configuration

4.5.1 Quadrupole avoided level-crossing data

The avoided quadrupole level-crossing technique was exploited during the experimental work on a powder sample of BeO in order to eliminate any axis dependence. The powder sample had to be held in a titanium compartment which meant that we had to take new background measurements with titanium rather than silver. Nonetheless the following plots are already accounted for this background. The goal of this experiment was to gather information about the relative distance between the muon particle and the nearest ^{9}Be nuclei. With this in mind, at a temperature of 12 K, a longitudinal magnetic field was swept from 0 up to 155 G with a 2.5 G step and from that point on with a 5 G step until 240 G. As for the repolarization measurements, these longitudinal field data were analyzed with two relaxing components (Eq. 4.4). The corresponding fractions of the slowly relaxing and the fast relaxing components are shown in a semilogarithmic plot in Fig. 4.24. The total signal is shown with a linear plot in Fig. 4.25.

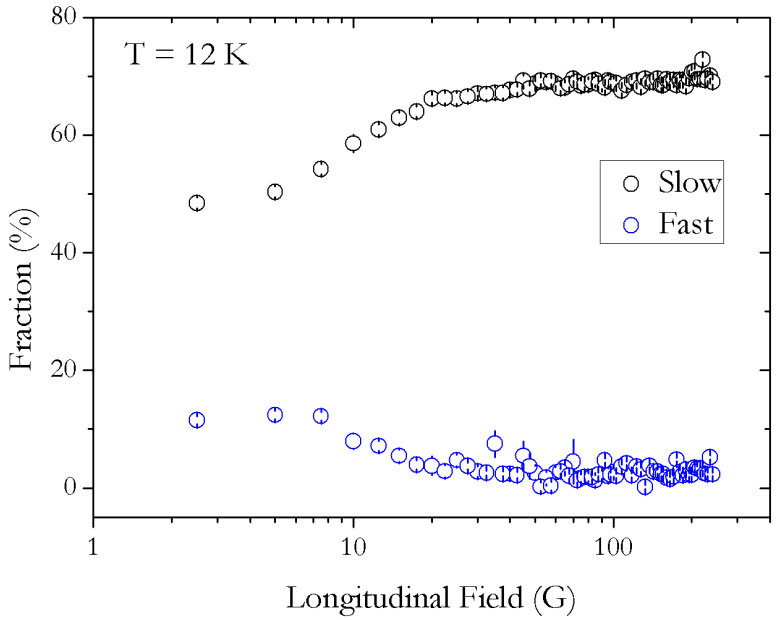

Figure 4.24: Repolarization measurements for low fields at a temperature of 12 K (logarithmic horizontal scale).

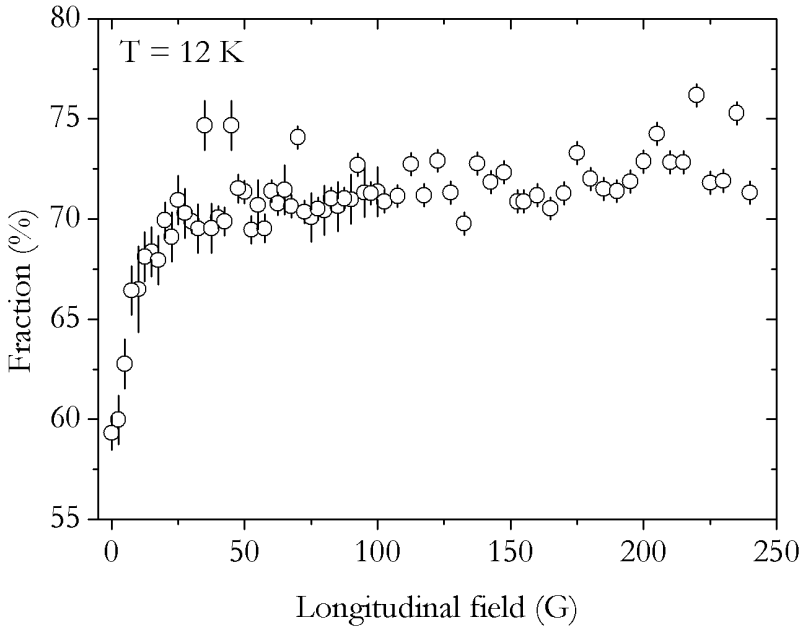

Figure 4.25: Repolarization measurements for low fields at a temperature of 12 K (linear horizontal scale).

No dip is observed for the slow component meaning that either the resonance effect is taking place for a longitudinal field higher than 240 G or the dip is too broad and therefore unobservable. The behavior below 20 G is nevertheless a sign of a possible

decoupling of the quadrupole interaction.

4.5.2 Simulations

In order to analyze these data we proceeded similarly as we did for section 3.2.1. We used James Lord's *Quantum* subroutine [Lor06] of the *Mantid* software [ABB+14]. Unlike in section 3.2.1, we now intended to extract the parameters from existing data instead of inputting them which implied several simulations. Therefore we made use of a script called *CreateBlankTableForQuantum v.1.* With this we were able to create a table in which we would initialize our parameters to sensible values. These were the same as in the wizard simulations from section 3.2.1: coordinates of muonium and the neighboring ^{9}Be nucleus, corresponding isotropic and anisotropic hyperfine frequencies, the quadrupole frequency of ^{9}Be and the longitudinal magnetic field loop. Then with the help of another script called *QuantumTableDrivenSimulation v.1* we were able to simulate the environment of the particle using our previously defined table. We started by varying the position of the ^{9}Be nucleus relative to the muon. The results of this variation are depicted in figure 4.26. It is evident that the distance between the ^{9}Be particle and the muon affects the initial polarized fraction. By figuring the ratio between the initial and final repolarized fractions in Fig. 4.25 ($\frac{58\%}{72\%} \sim 0.8$) we were able to find the most appropriate value in our distance fit, which turned out to be 1.3 $\mathring{A}$.

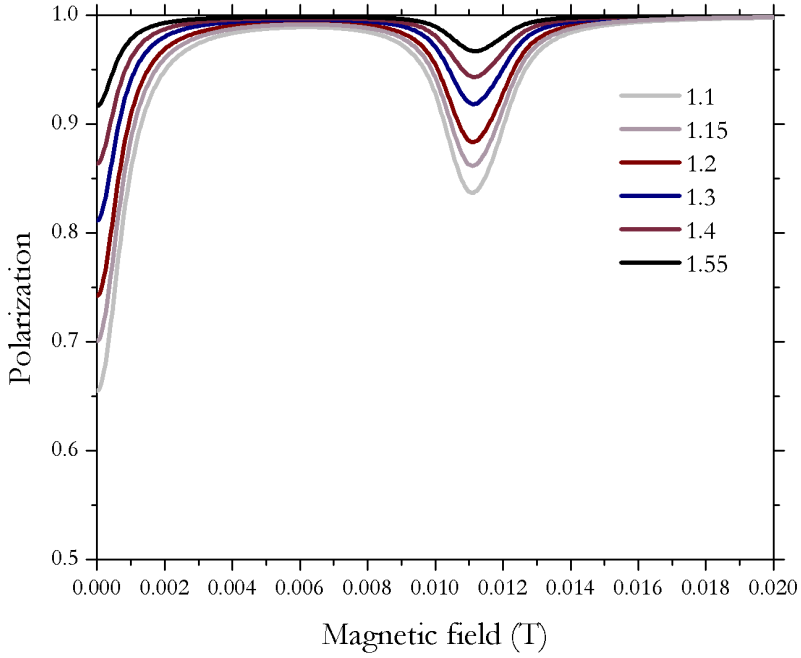

Figure 4.26: Simulation of the BeO quadrupole avoided level-crossing spectra regarding the distance in $\mathring{A}$ between the relative positions of the muon and its nearest ^{9}Be neighbor.

We then fixed this distance and attempted to find the quadrupole frequency that better defined our data (Fig. 4.25). The dip became more prolonged, less pronounced and manifested for higher fields as we increased the quadrupole moment which is evident in figure 4.27. Since our results did not exhibit any dip in polarization until 250 G all we can say is that the quadrupole frequency must be, at least 1.3 μs^{-1}.

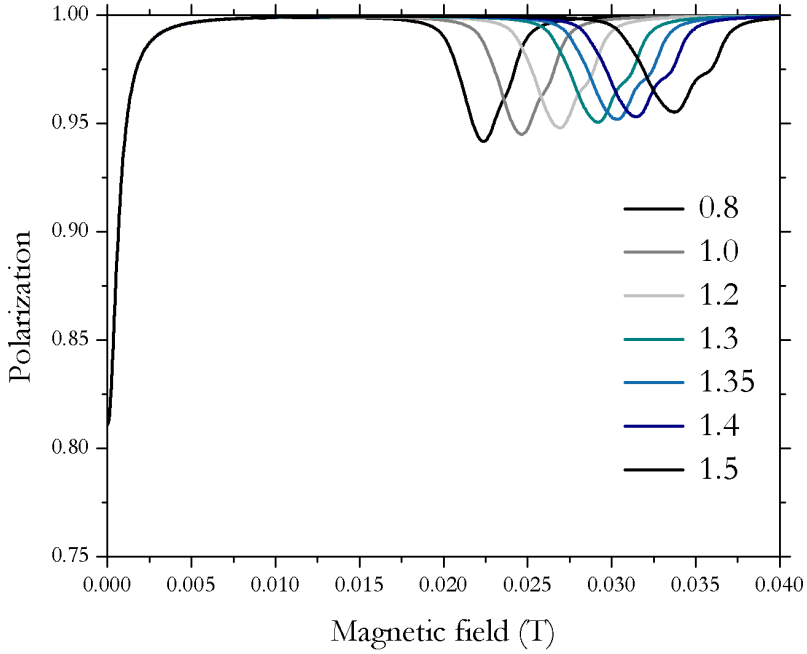

Figure 4.27: Simulation of the BeO quadrupole avoided level-crossing spectra regarding the quadrupole frequency in μs^{-1} of the ^{9}Be nucleus.

The dip must be at an unexpectedly high field, taking into account usual values (for example the quadrupole avoided level-crossing value for Cu shows a dip around 75 G, see Fig. 3.4). We hypothesize that several ^{9}Be nuclei are significantly involved. This would broaden the dip, eventually turning it unobservable. Simulations with several ^{9}Be nuclei are suggested as a future work (see section 5.1).

4.6 Discussion

4.6.1 The current model for muonium formation in oxides

A model has been proposed by Vilão et al that aims to explain the final configurations of muonium in oxides [VVA^{+}17]. As mentioned in section 2.1.1 muons are initially implanted into the material with an energy of 4 MeV. Before thermalization, the muon will go through several stages: As energies are high, the muon will experience an electrostatic interaction causing it to shed some of its energy. This is described by the Bethe-Bloch theory [Leo94]. During this process the interaction is

purely electrostatic thus, no spin dynamics are involved. This means that the initial polarization of the muon is kept. The time this stage takes is dependent on the material. For solid silicon studies have shown this to be around 10 ps [Pat88]. For energies around 35 keV the muon particle and the valence electrons reach similar velocities. Here a charge exchange cycle takes place, during which muonium can be formed. This stage takes most of the energy from the muons, leaving them with tens of eV [Vil07].

According to the model of Vilão et al [VVA$^+$17][VVA$^+$18], at the final stage of thermalization, muonium is converted to one of these final states: interstitial muonium also called atomic or atom-like muonium (Mu^0_{atom}), bound muonium (Mu^0_{bound}) and bound muon (Mu^+_{bound}). The model is schematized in Fig. 4.28. Muons thermalizing as Mu^+ immediately bind to oxygen, forming the Mu^+_{bound} configuration. The muonium route however has more intricacies. This model assumes that muonium goes through a transition state before reaching a stable configuration. This transition state is characterized by a weak hyperfine interaction and thus exhibits a diamagnetic-like behavior. When muonium reaches this state only two possibilities lead to a stable configuration:

1. If the remaining energy of the particle is dispersed as phonon excitations through the lattice. When this happens, muonium reaches its ground state, forming (Mu^0_{atom}).

2. Alternatively the remaining energy of muonium can be used to overcome the small energy barrier for forming the bound configuration. When this happens muonium reaches the Mu^0_{bound} state.

At low temperatures phonon dispersion is difficult because the lattice is rigid and hardly relaxes. Also, it is possible that when overcoming the barrier to form the bound configuration, the electron is lost and a diamagnetic Mu^+_{bound} state is formed instead of the Mu^0_{bound} configuration. In some cases the Mu^0_{atom} configuration may be formed promptly, bypassing the transition state altogether [dSMV$^+$16].

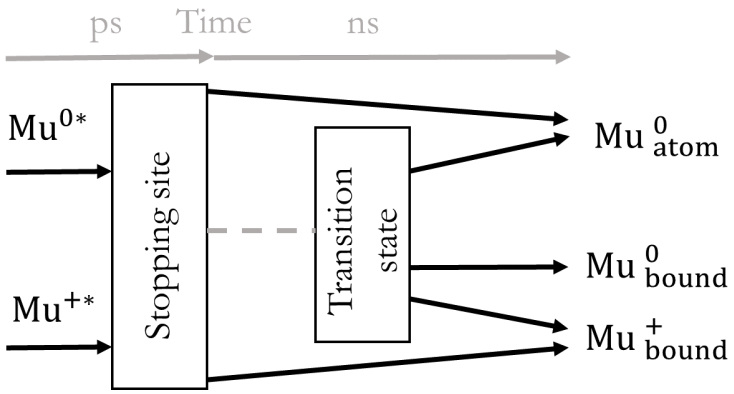

Figure 4.28: The muon and muonium conversion paths. The * denotes epithermal Mu^0/Mu^+ states of the charge-exchange cycle. Positive muons are immediately bound to the lattice but muonium goes through a transition state that leads it to different configurations. Adapted from [VVA+17].

The following figure (Fig. 4.29) describes the muonium route with more detail using a saddle potential profile [VVA+18]. In this figure we can distinguish three different muonium configurations:

1. The black arrow which represents the case in which the transition state is bypassed forming the prompt atomic muonium state (Mu^0_{atom}).

2. The blue arrow which represents the case in which muonium goes through the transition state but manages to convert its remaining energy via lattice relaxation and reach a delayed atomic muonium state (Mu^0_{atom}).

3. The red arrow which represents the previously described bound muonium state Mu^0_{bound} which may lose its electron and form the Mu^+_{bound} state.

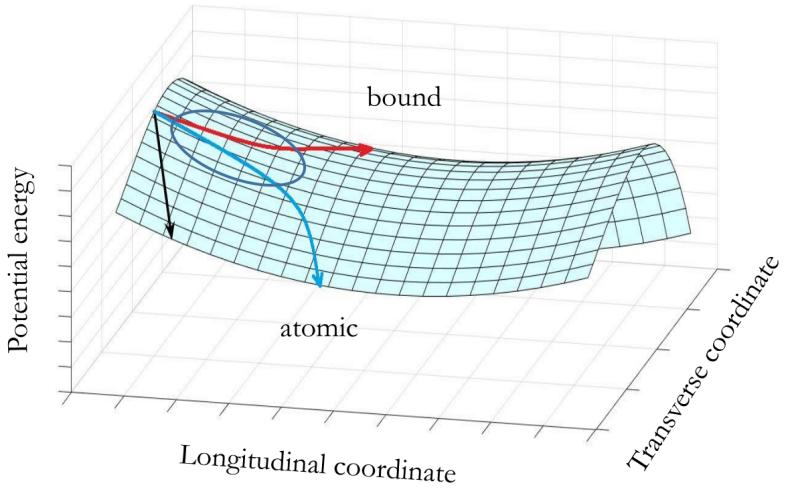

Figure 4.29: The saddle potential profile. The muonium trajectories (black, blue and red arrows) correspond to prompt atomic muonium and delayed atomic muonium (Mu^0_{atom}) and bound muonium (Mu^0_{bound}) state, respectively [VVA+18].

The starting point of the configurations is determined by the initial potential of the particle at the unrelaxed lattice. Muonium must overcome the energy barrier to reach the stable Mu^0_{bound} configuration (red line). In the figure, this is analogous to climbing the saddle potential. The blue encircled area represents the transition state which the delayed atomic muonium state (Mu^0_{atom}) and the bound muonium state (Mu^0_{bound}) go through.

Projecting the saddle on its transverse coordinate helps visualizing the potential barrier. This is illustrated in figure 4.30. It is important to bear in mind that the the saddle analogy (Fig. 4.29) is only valid for the potential around the barrier.

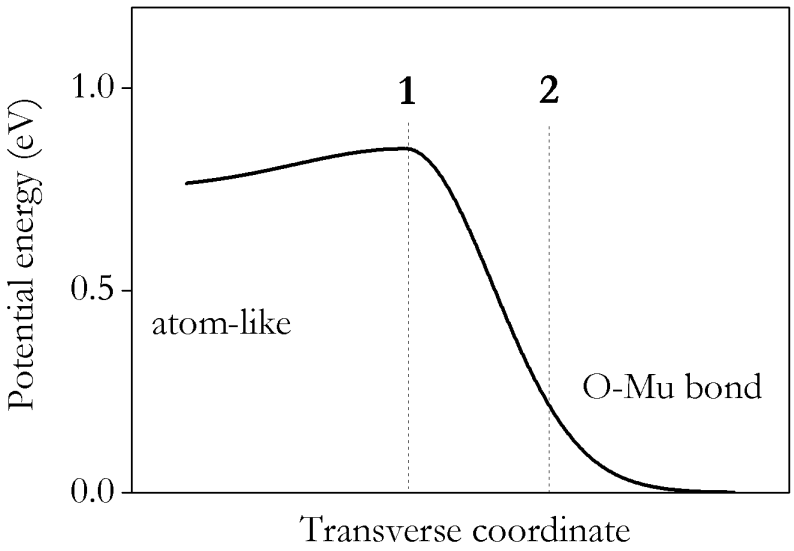

Figure 4.30: The extended transverse coordinate projection from the saddle potential profile. The energy barrier for the bound configuration is clear in point 1. The formation of the bound configuration is represented by point 2. Extracted from [VVA+17].

4.6.2 Characterization of the slow fraction

We assign the slowly relaxing diamagnetic component observed in the transverse field measurements (Fig. 4.7) and in the repolarization measurements (Figs. 4.16 and 4.17) to the muon configuration bound to an oxygen (Figs 1.5 or 1.6). The van Vleck relaxations are also consistent with Mu^+ states (table 4.1) and preclude that this component corresponds to a neutral Mu^0 configuration.

At temperatures around 150 K, a prompt diamagnetic signal could not explain the drop in the slow fraction with increasing temperature (Fig. 4.7). This could be a manifestation of a thermal spike effect which can be explained in the following way [Wei]: After the aforementioned charge exchange cycle the remaining energy of muonium can not be easily dissipated. This is due to temperatures being low which makes it difficult for the lattice to dissipate the additional energy brought by the epithermal muon. It becomes then possible for muonium to reach a stable state by overcoming the energy barrier necessary to form the bound configuration. During this process muonium loses its electron forming the Mu^+_{bound} state and therefore contributing to the diamagnetic signal (lower route of Fig. 4.28 or red arrow in

Fig. 4.29). The phase of the diamagnetic signal remains constant because the contribution of the prompt diamagnetic fraction is dominant and thus the expected phase shift from the converted muons becomes negligible (Fig. 4.11).

As temperature increases past 150 K the slow fraction starts to drop in favor of the missing fraction. We attribute this to the quenching of the transition state in favor of the formation of prompt atomic muonium. The formation of the delayed Mu^{+}_{bound} bound configuration and of the fast component is thus gradually eradicated which results in a decrease of the diamagnetic signal.

The Boltzmann fit for the transverse field measurements (Fig. 4.13) describes the barrier as rather small (0.13 eV). However the thermal spike is not a pure Boltzmann process as that described by equation 4.3. A. Weidinger has proposed a model to describe this thermal spike effect [Wei]. According to this model, the remaining energy trapped in the muonium site will contribute to an effective temperature. In practice this is a correction to temperature on equation 4.3. The temperature is therefore redefined as:

$$T_{\text{eff}} = T + T_{\mu} e^{-cT} \tag{4.5}$$

Where

- T_{μ} is the remaining energy from the charge exchange cycle in K;
- c is a parameter associated with thermal conductivity;
- T_{eff} the effective temperature experienced by the particle;

Leaving equation 4.3 as such:

$$f_d = \frac{f_0}{1 + N^{-E_a/k_B T_{\text{eff}}}} + B \tag{4.6}$$

This model describes the conversion of the transition state to the diamagnetic state by overcoming an energy barrier E_a. The thermal spike effect is included by admitting an effective temperature T_{eff} which decays exponentially to the lattice temperature T with a constant c.

We note that in figure 4.13 we do not observe the expected recovering of the diamagnetic fraction with temperature up to 700 K. The thermal spike decay at low temperatures is nevertheless an indication of the presence of such a barrier, implying that a recovery of the diamagnetic fraction is expected at T> 700 K (with a corresponding Ea, more on this in section 5.1). This makes it so fitting equation 4.6 becomes difficult and with error bars comparable to the parameters themselves. The curve in figure 4.31 is therefore more of a simulation rather than a fit.

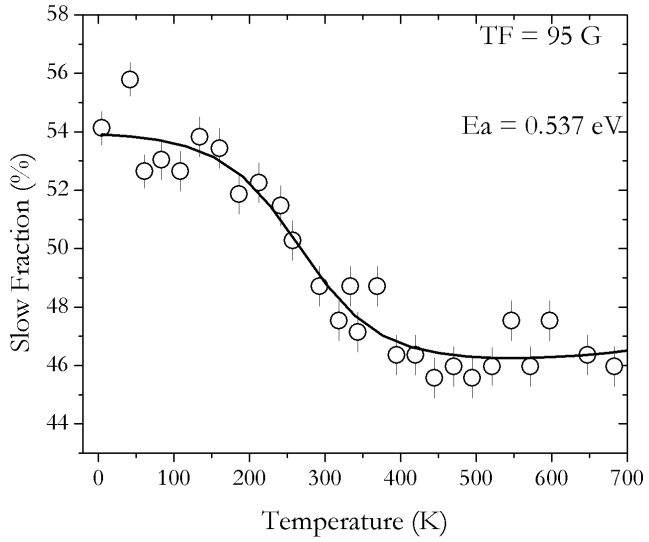

Figure 4.31: The fitted function using A. Weidinger's model for the thermal spike effect.

The following parameters were obtained

- $T_\mu = 3836.21$ K
- $c = 5.55 \times 10^{-3}$ K^{-1}
- $E_a = 0.537$ eV
- $N = 247$
- $B = 45.87$ %

4.6.3 Characterization of the fast fraction

For the repolarization measurements (Figs. 4.18 and 4.17) the fast fractions disappears around the first step. This is an indication that the first repolarization step is associated with the fast fraction. Judging from the admittedly low fitted hyperfine interactions we conclude that the fast fraction must be associated with a weakly bound paramagnetic state. Therefore we argue that this signal corresponds to muonium in the transition state.

As previously explained, **at low temperatures** muonium can not reach its ground state due to an unrelaxed lattice. Muonium in the excited lattice has a lower hyperfine interaction than in its ground state and thus can be picked up by the HiFi instrument. **At high temperatures**, the transverse field measurements show that the transition state becomes quenched (Fig. 4.8). This is because the lattice is now able to relax which allows muonium to promptly reach its ground state: atomic muonium. This state has a large hyperfine interaction and thus is not detectable constituting a missing fraction at ISIS.

4.6.4 Characterization of the missing fraction

For low temperatures, the big contributor to the missing fraction is the interstitial muonium. This is supported by the repolarization measurements for low temperatures which fit to a hyperfine interaction typical of interstitial muonium (Figs. 4.17 and Fig. 4.19). Besides, GPS measurements performed at 6 K also confirmed the presence of the particle [MVV+17]. **For high temperatures** the transition state starts to disappear (Fig. 4.8). This means that less delayed atomic Mu^{0}_{atom} and bound muon(ium) $Mu^{+(0)}_{bound}$ is formed in favor of prompt atomic muonium. Seeing as this configuration has a high hyperfine interaction its precession can not be picked up by the HiFi instrument and therefore its signal constitutes a missing fraction.

5

Conclusions

In this work we have investigated the microscopic configurations of hydrogen using the positive muon as a light pseudo-isotope. We have identified two base configurations:

- An oxygen bound configuration (corresponding to the slow diamagnetic component observed in the muon spin spectroscopy results) that corresponds to the muon sitting in a donor state such as that proposed theoretically by A. Marinopoulos (Figs. 1.5 and 1.6) [MVV$^+$17]. Only the positively charged configuration is observed, and not any neutral version [VMV$^+$11].

- A deep atomic-like configuration (corresponding to the muonium state observed directly in the PSI experiments and indirectly at ISIS through the repolarization measurements) that corresponds to the muon sitting in an acceptor site such as that calculated by A. Marinopoulos [MVV$^+$17] and shown in figure 1.7.

The concomitant observation of these two configurations is itself a sign of their metastability, pointing to a compensating nature of H in BeO, as predicted in [MVV$^+$17]. Furthermore, regarding the positively charged configuration, we observed consistent results with the *ab-initio* calculations, possibly with an anti-bonding site. This means that at low temperature values, during the time of the μSR experiment, the lattice does not have time to relax to the ground state configuration. This leads us to another important set of conclusions regarding the applicability of the muon spin spectroscopy technique and the violent implantation

of positive muons, leading to a possibly unfinished thermalization process:

- A fast relaxing component was also identified in terms of a short-lived muonium precursor state with a low hyperfine interaction.
- The possible presence of a thermal spike effect affecting the final yield of the observed configurations, particularly at low temperatures.

We conclude that the thermalization process is extremely important to the correct interpretation of the μSR data in BeO. This process exhibits an unusually slow timescale which we attribute to the extreme insulating character of the material. More than a hindrance, this may become an opportunity for using the muon spin spectroscopy technique to probe microscopic processes triggered by the injection of an energetic particle in a solid, such as those related to the important fields of microscale and nanoscale heat transfer [SP08].

5.1 Future perspectives

This works constitutes a necessary first step in the microscopic characterization of hydrogen configurations and dynamics in BeO, but several questions were raised in the course of this investigation that require further clarification in future works.

5.1.1 Extension of the temperature dependent studies

A future proposal at ISIS could be based around the idea of extending the temperature dependent studies up to the limit of the reflector furnace (1500 K). This would result in a wider temperature dependency scope of the diamagnetic signal also allowing us to characterize an activation energy. Having said this, figure 5.1 is the extended version of the simulation of the thermal spike effect (Fig. 4.31) and what we expected to see for a wider temperature range[1]. If the thermal spike model is correct, we expect to see a significant recovery of the diamagnetic fraction up to

[1] not considering the ionization from the interstitial state

1500 K.

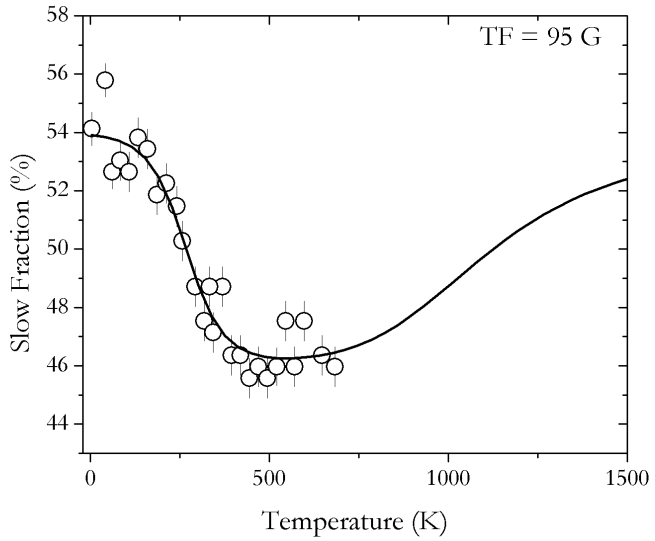

Figure 5.1: The thermal spike simulation from figure 4.31 extended for higher temperatures.

5.1.2 Additional level crossing measurements and modeling

The level crossing measurements were performed up to 240 G at 12 K. The typical dip was not observed which could mean that it lies at higher fields. However, before proposing additional measurements it seems important to extend the simulations in order to include additional ^{9}Be nuclei. These could also provide a better explanation for the observed avoided quadrupole level-crossing pattern. The ground state of the diamagnetic configuration may not be manifested due to the low temperature at which the experiment was performed. We therefore propose another quadrupole avoided level-crossing experiment around room temperature, where we expect the muon to be able to reach its ground state.

5.1.3 Clarification of muonium dynamics

The stable isotropic muonium repolarization function is clearly not enough to characterize the behavior exhibited by the high field step in the repolarization measure-

ments (Fig. 4.17). Furthermore, the transition state muonium exhibits particularly additional dynamics for some temperatures (Figs. 5.2). Investigating these anomalies would require a new longitudinal field run altogether, with a smaller step and increased statistics.

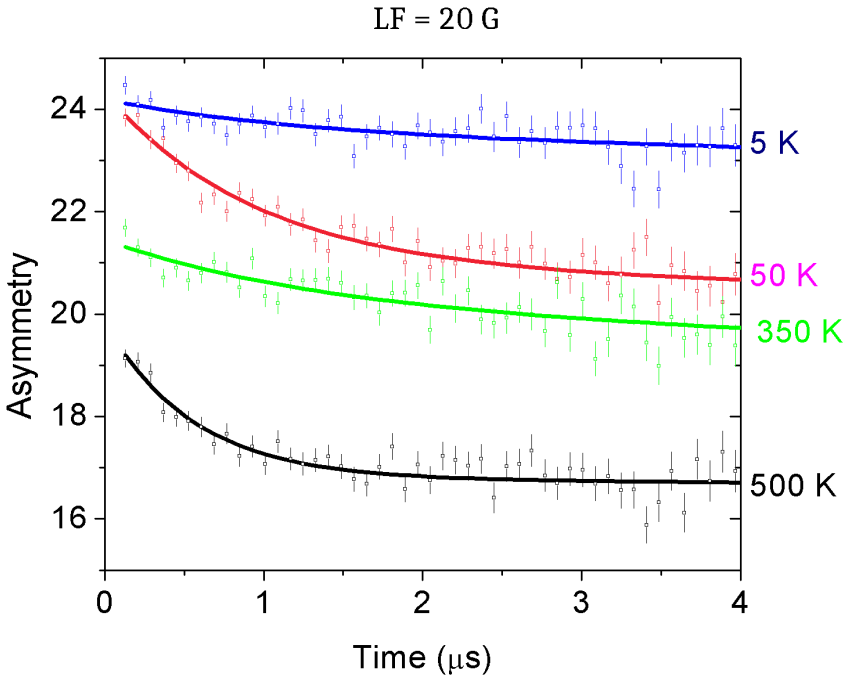

Figure 5.2: The time spectra of a few selected temperatures for a 20 G longitudinal field run.

5.1.4 Generalizing the thermal spike model to other systems

It is possible that other materials whose data has already been studied and published may have manifested a thermal spike effect. When considering the temperature dependency measurements of the diamagnetic fraction depicted in figure 5.3, Bi_2O_3 exhibits a very similar behavior to that of the simulated thermal spike profile 5.1. The thermal spike model is still in its infancy and no analysis with it in mind has been made whatsoever. We therefore suggest reanalyzing these Bi_2O_3 data and eventually extending the temperature dependency measurements for higher values.

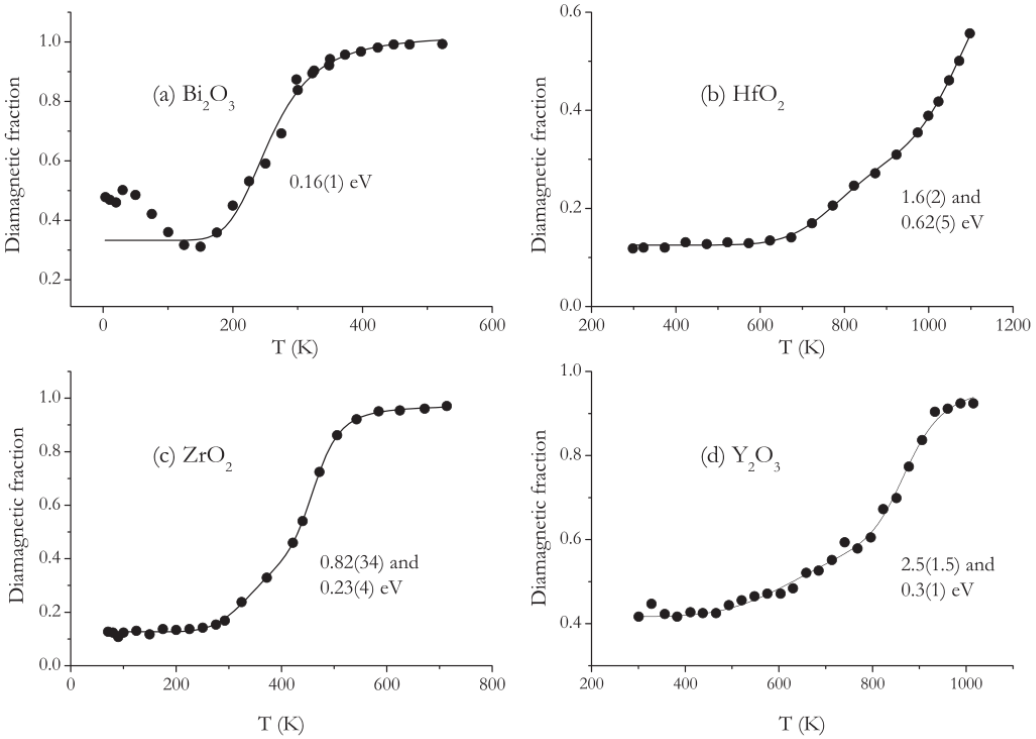

Figure 5.3: The diamagnetic fraction dependency with temperature for several materials: a) Bi_2O_3 b)Hf_2O_3 c) ZrO_2 d) Y_2O_3. Extracted from [CGL+06]

Bibliography

[ABB+14] O. Arnold, J.C. Bilheux, J.M. Borreguero, A. Buts, S.I. Campbell, L. Chapon, M. Doucet, N. Draper, R. Ferraz Leal, M.A. Gigg, V.E. Lynch, A. Markvardsen, D.J. Mikkelson, R.L. Mikkelson, R. Miller, K. Palmen, P. Parker, G. Passos, T.G. Perring, P.F. Peterson, S. Ren, M.A. Reuter, A.T. Savici, J.W. Taylor, R.J. Taylor, R. Tolchenov, W. Zhou, and J. Zikovsky. Mantid—data analysis and visualization package for neutron scattering and μsr experiments. *Nuclear Instruments and Methods in Physics Research Section A: Accelerators, Spectrometers, Detectors and Associated Equipment*, 764:156–166, 2014.

[Abr84] Anatole Abragam. Resonance magnetic - spectrometrie par croisments de niveuax en physique du muon. *Comptes rendus de l'Académie des sciences*, 299:95–99, May 1984.

[Alb17] Marco Alberto. High dielectric constant oxides for cmos technology, 2017.

[Blu99] S. J. Blundell. Spin-polarized muons in condensed matter physics. *Contemporary Physics*, 40(3):175–192, 1999.

[CGL+06] S F J Cox, J L Gavartin, J S Lord, S P Cottrell, J M Gil, H V Alberto, J Piroto Duarte, R C Vilão, N Ayres de Campos, D J Keeble, E A Davis, M Charlton, and D P van der Werf. Oxide muonics: II. modelling the electrical activity of hydrogen in wide-gap and high-permittivity dielectrics. *Journal of Physics: Condensed Matter*, 18(3):1079, 2006.

[CGR+77] M. Camani, F. N. Gygax, W. Rüegg, A. Schenck, and H. Schilling. Positive muons in copper: Detection of an electric-field gradient at the neighbor cu nuclei and determination of the site of localization. *Phys. Rev. Lett.*, 39:836–839, Sep 1977.

[CLL+13] S F J Cox, R L Lichti, J S Lord, E A Davis, R C Vilão, J M Gil, T D Veal, and Y G Celebi. The first 25 years of semiconductor muonics at isis, modelling the electrical activity of hydrogen in inorganic semiconductors and high-k dielectrics. *Physica Scripta*, 88(6):068503, 2013.

[Cox92] S. F. J. Cox. Detection of quadrupole interactions by muon level crossing resonance. *Zeitschrift für Naturforschung A*, 47:371–381, 1992.

[dSMV+16] E. Lora da Silva, A. G. Marinopoulos, R. B. L. Vieira, R. C. Vilão, H. V. Alberto, J. M. Gil, R. L. Lichti, P. W. Mengyan, and B. B. Baker. Electronic structure of interstitial hydrogen in lutetium oxide from DFT$+u$ calculations and comparison study with μSR spectroscopy. *Phys. Rev. B*, 94:014104, Jul 2016.

[dWC00] Van de Walle and G. Chris. Hydrogen as a cause of doping in zinc oxide. *Phys. Rev. Lett.*, 85:1012–1015, Jul 2000.

[dWCN03] Van de Walle, G. Chris, and J. Neugebauer. Universal alignment of hydrogen levels in semiconductors, insulators and solutions. *Nature*, 423:626, 2003.

[GMF+99] J. M. Gil, P. J. Mendes, L. P. Ferreira, H. V. Alberto, R. C. Vilao, N. Ayres de Campos, A. Weidinger, Y. Tomm, Ch. Niedermayer, M. V. Yakushev, R. D. Tomlinson, S. P. Cottrell, and S. F. J. Cox. Modeling hydrogen in $CuInSe_2$ and $CuInS_2$ solar cell materials using implanted muons. *Phys. Rev. B*, 59:1912–1916, Jan 1999.

[Hil14a] Adrian Hillier. Muon spectroscopy. *ISIS muon training*, 2014.

[Hil14b] Adrian Hillier. Welcome. *ISIS muon training*, 2014.

[Hou03] Michel Houssa. High k gate dielectrics. 2003.

[JYH+14] Derek W. Johnson, Jung Hwan Yum, Todd W. Hudnall, Ryan M. Mushinski, Christopher W. Bielawski, John C. Roberts, Wei-E Wang, Sanjay K. Banerjee, and H. Rusty Harris. Characterization of ald beryllium oxide as a potential high-k gate dielectric for low-leakage AlGaN/GaN MOSHEMTs. *Journal of Electronic Materials*, 43(1):151–154, Jan 2014.

[KR95] S.R. Kreitzman and E. Roduner. Theory of avoided level-crossing relaxation dynamics for axial muonated radicals. *Chemical Physics*, 192(3):189 – 230, 1995.

[LBK+91] G. M. Luke, J. H. Brewer, S. R. Kreitzman, D. R. Noakes, M. Celio, R. Kadono, and E. J. Ansaldo. Muon diffusion and spin dynamics in copper. *Phys. Rev. B*, 43:3284–3297, Feb 1991.

[LBP13] Tom Lancaster, Stephen J Blundell, and Francis L Pratt. Another dimension: investigations of molecular magnetism using muon–spin relaxation. *Physica Scripta*, 88(6):068506, 2013.

[Leo94] W. R. Leo. Techniques for nuclear and particle physics experiments. 1994.

[Lor06] J.S. Lord. Computer simulation of muon spin evolution. *Physica B: Condensed Matter*, 374-375:472 – 474, 2006. Proceedings of the Tenth International Conference on Muon Spin Rotation, Relaxation and Resonance.

[MBC+13] J S Möller, P Bonfà, D Ceresoli, F Bernardini, S J Blundell, T Lancaster, R De Renzi, N Marzari, I Watanabe, S Sulaiman, and M I Mohamed-Ibrahim. Playing quantum hide-and-seek with the muon: localizing muon stopping sites. *Physica Scripta*, 88(6):068510, 2013.

[Moo65] Gordon Moore. Craming more components onto integrated circuits. 1965.

[MVV+17] A. G. Marinopoulos, R. C. Vilão, R. B. L. Vieira, H. V. Alberto, J. M. Gil, M. V. Yakushev, R. Scheuermann, and T. Goko. Defect levels and hyperfine constants of hydrogen in beryllium oxide from hybrid-functional calculations and muonium spectroscopy. *Philosophical Magazine*, 97(24):2108–2128, 2017.

[Pat88] Bruce D. Patterson. Muonium states in semiconductors. *Rev. Mod. Phys.*, 60:69–159, Jan 1988.

[Per11] Paul Percival. Lecture 9. *TRIUMF summer institute*, 2011.

[Pra00] F.L Pratt. Wimda: a muon data analysis program for the windows pc. *Physica B: Condensed Matter*, 289-290:710 – 714, 2000.

[Ren14] Roberto Renzi. Introduction to μSR. *ISIS muon training*, 2014.

[RF06] J. Robertson and B. Falabretti. Band offsets of high k gate oxides on III-V semiconductors. *Journal of Applied Physics*, 100(1):014111, 2006.

[RPM+95] Emil Roduner, Kosmas Prassides, Roderick M. Macrae, Ian M. Thomas, Christof Niedermayer, Ulrich Binninger, Christian Bernhard, Anselm Hofer, and Ivan D. Reid. Reorientational dynamics of C_{60} in the solid state. an avoided level-crossing muon spin resonance study. *Chemical Physics*, 192(3):231 – 237, 1995.

[Rub16] Roy Rubenstein. Altera's 30 billion transistor fpga. *Gazettabyte*, 2016.

[Sch85] A. Schenck. Muon spin rotation spectroscopy: Principles and applications in solid state physics. 1985.

[Sch15] Bill Schweber. Moore's law at 50. *Globalspec*, 2015.

[Sim13] Steven H. Simon. The oxford solid state basics. 2013.

[Sim16a] Tom Simonite. Intel puts the breaks on moore's law. *MIT Technology review*, 2016.

[Sim16b] Tom Simonite. Moore's law is dead, now what? *MIT Technology review*, 2016.

[SP08] C. B. Sobhan and G. P. Peterson. Microscale and nanoscale heat transfer fundamentals and engineering applications. 2008.

[SW95] Gunter Schatz and Alois Weidinger. Nuclear condensed matter physics: nuclear methods and applications. 1995.

[Uem98] Y J Uemura. Nato School. μsr relaxation function in magnetic materials. 1998.

[Vie18] Ricardo Vieira. Hydrogen in high-k permittivity oxides modelled by the muon analogue. 2018.

[Vil98] R C Vilão. Hidrogénio e muões em calcopirites usadas em células solares. *Relatório da disciplina de Seminário*, 1998.

[Vil07] Rui Vilao. Isolated hydrogen in II−VI zinc-chalcogenide widegap semiconductors modelled by the muon analogue, 2007.

[VMV+11] R. C. Vilao, A. G. Marinopoulos, R. B. L. Vieira, A. Weidinger, H. V. Alberto, J. Piroto Duarte, J. M. Gil, J. S. Lord, and S. F. J. Cox. Hydrogen impurity in paratellurite α-TeO_2: Muon-spin rotation and ab initio studies. *Phys. Rev. B*, 84:045201, July 2011.

[VVA+17] R. C. Vilao, R. B. L. Vieira, H. V. Alberto, J. M. Gil, and A. Weidinger. Role of the transition state in muon implantation. *Phys. Rev. B*, 96:195205, Nov 2017.

[VVA+18] R C Vilao, R B L Vieira, H V Alberto, J M Gil, A Weidinger, R. L. Lichti, P. W. Mengyan, B. B. Baker, and J. S. Lord. The barrier model in muon implantation and application to Lu_2O_3. *submitted to Physical review B*, 2018.

[Wei] Alois Weidinger. Private communication.

[WWA01] G. D. Wilk, R. M. Wallace, and J. M. Anthony. High- k gate dielectrics: Current status and materials properties considerations. *Journal of applied physics*, 89(10):5243, 2001.

[XRGC05] K. Xiong, J. Robertson, M. C. Gibson, and S. J. Clark. Defect energy levels in HfO_2 high-dielectric-constant gate oxide. *Applied Physics Letters*, 87(18):183505, 2005.

[YBH+14] J. H. Yum, S.K. Banerjee, Todd W. Hudnall, C. W. Bielawski, Lanford W.A., French B.L., P. Henry, H. Li, M. Kuhn, and S.W. King. Investigation of atomic layer deposited beryllium oxide material properties for high-k dielectric applications. *J. Vac. Sci. Technol. B*, 32:03D117, 2014.

[YSH+12] J. H. Yum, H. S. Shin, R. Hill, J. Oh, H. D. Lee, Ryan M. Mushinski, Todd W. Hudnall, C. W. Bielawski, S. K. Banerjee, W. Y. Loh, Wei-E Wang, and Paul Kirsch. A study of capping layers for sulfur monolayer doping on III−V junctions. *Applied Physics Letters*, 101(25):253514, 2012.

Appendices

A

Distances between the relative position of the muon and the neighboring nuclei

	Distance between the relative position of the muon site and the neighbor (Å)			
Neighbour index	$H^+-OH_{\|\|}$	$H^+-ABO_\perp$	$H^+-OH_\perp$	$H^+-ABO_{\|\|}$
1	1.7338	1.7318	1.6639	1.7175145
2	2.0911	1.7344	1.778	1.7832252
3	2.096	1.9421	1.9717	1.7886323
4	2.1003	2.6859	2.2042	1.792055
5	2.8219	2.8564	2.2712	2.7094978
6	2.8253	3.1866	2.3689	3.14201
7	2.8264	3.2049	2.842	3.1443671
8	2.833	3.2062	3.1476	3.1533257
9	2.8343	–	3.1478	3.1682485
10	2.8375	–	2.8375	3.168447
11	–	–	–	3.173972
12	–	–	–	3.1740442
13	–	–	–	3.1794904
14	–	–	–	3.1798027

Table A.1: The table cointaing the distances between the relative position of the muon and the neighboring nucleus for the different states introduced in section 1.3. These values were provided by A. Marinopoulos and used in the calculation of the relaxation values in the van Vleck limit in section 4.3.2.